

A PHYSICAL MODEL FOR THE EVOLVING ULTRAVIOLET LUMINOSITY FUNCTION OF HIGH REDSHIFT GALAXIES AND THEIR CONTRIBUTION TO THE COSMIC REIONIZATION

ZHEN-YI CAI^{1,2}, ANDREA LAPI^{1,3}, ALESSANDRO BRESSAN¹, GIANFRANCO DE ZOTTI^{1,4}, MATTIA NEGRELLO⁴, AND LUIGI DANESE¹

¹ Astrophysics Sector, SISSA, Via Bonomea 265, I-34136 Trieste, Italy; zcai@sissa.it

² Department of Astronomy and Institute of Theoretical Physics and Astrophysics, Xiamen University, Xiamen 361005, China

³ Dipartimento di Fisica, Università “Tor Vergata,” Via della Ricerca Scientifica 1, I-00133 Roma, Italy

⁴ INAF–Osservatorio Astronomico di Padova, Vicolo dell’Osservatorio 5, I-35122 Padova, Italy

Received 2013 July 1; accepted 2014 February 27; published 2014 March 26

ABSTRACT

We present a physical model for the evolution of the ultraviolet (UV) luminosity function of high-redshift galaxies, taking into account in a self-consistent way their chemical evolution and the associated evolution of dust extinction. Dust extinction is found to increase fast with halo mass. A strong correlation between dust attenuation and halo/stellar mass for UV selected high- z galaxies is thus predicted. The model yields good fits of the UV and Lyman- α ($\text{Ly}\alpha$) line luminosity functions at all redshifts at which they have been measured. The weak observed evolution of both luminosity functions between $z = 2$ and $z = 6$ is explained as the combined effect of the negative evolution of the halo mass function; of the increase with redshift of the star formation efficiency due to the faster gas cooling; and of dust extinction, differential with halo mass. The slope of the faint end of the UV luminosity function is found to steepen with increasing redshift, implying that low luminosity galaxies increasingly dominate the contribution to the UV background at higher and higher redshifts. The observed range of the UV luminosities at high z implies a minimum halo mass capable of hosting active star formation $M_{\text{crit}} \lesssim 10^{9.8} M_{\odot}$, which is consistent with the constraints from hydrodynamical simulations. From fits of $\text{Ly}\alpha$ line luminosity functions, plus data on the luminosity dependence of extinction, and from the measured ratios of non-ionizing UV to Lyman-continuum flux density for samples of $z \simeq 3$ Lyman break galaxies and $\text{Ly}\alpha$ emitters, we derive a simple relationship between the escape fraction of ionizing photons and the star formation rate. It implies that the escape fraction is larger for low-mass galaxies, which are almost dust-free and have lower gas column densities. Galaxies already represented in the UV luminosity function ($M_{\text{UV}} \lesssim -18$) can keep the universe fully ionized up to $z \simeq 6$. This is consistent with (uncertain) data pointing to a rapid drop of the ionization degree above $z \simeq 6$, such as indications of a decrease of the comoving emission rate of ionizing photons at $z \simeq 6$, a decrease of sizes of quasar near zones, and a possible decline of the $\text{Ly}\alpha$ transmission through the intergalactic medium at $z > 6$. On the other hand, the electron scattering optical depth, τ_{es} , inferred from cosmic microwave background (CMB) experiments favor an ionization degree close to unity up to $z \simeq 9$ – 10 . Consistency with CMB data can be achieved if $M_{\text{crit}} \simeq 10^{8.5} M_{\odot}$, implying that the UV luminosity functions extend to $M_{\text{UV}} \simeq -13$, although the corresponding τ_{es} is still on the low side of CMB-based estimates.

Key words: early universe – galaxies: evolution – galaxies: formation – galaxies: high-redshift – ultraviolet: galaxies

Online-only material: color figures

1. INTRODUCTION

One of the frontiers of present day astrophysical/cosmological research is the understanding of the transition from the “dark ages,” when the hydrogen was almost fully neutral, to the epoch when stars and galaxies began to shine and the intergalactic hydrogen was almost fully re-ionized. Observations with the Wide Field Camera 3 on the *Hubble Space Telescope* (Finkelstein et al. 2012; Bouwens et al. 2012; Oesch et al. 2013a, 2013b; Ellis et al. 2013; Robertson et al. 2013) have substantially improved the observational constraints on the abundance and properties of galaxies at cosmic ages of less than 1 Gyr. Determinations of the ultraviolet (UV) luminosity function (LF) of galaxies at $z = 7$ – 8 have been obtained by Bouwens et al. (2008, 2011b), Smit et al. (2012), Oesch et al. (2012), Schenker et al. (2013), McLure et al. (2010, 2013), Yan et al. (2011, 2012), Lorenzoni et al. (2011, 2013), and Bradley et al. (2012). Estimates over limited luminosity ranges were provided by Bouwens et al. (2008), Oesch et al. (2013a), and McLure et al. (2013) at $z = 9$, and by Bouwens et al. (2011b)

and Oesch et al. (2013a, 2013b) at $z = 10$. Constraints on the UV luminosity density at redshifts up to 12 have been presented by Ellis et al. (2013).

Because galaxies at $z \geq 6$ are the most likely sources of the UV photons capable of ionizing the intergalactic hydrogen, the study of the early evolution of the UV luminosity density is directly connected with the understanding of the cosmic reionization. Several studies (Robertson et al. 2013; Kuhlen & Faucher-Giguère 2012; Alvarez et al. 2012; Haardt & Madau 2012) have adopted parameterized models for the evolving UV luminosity density. These models are anchored to the observed high- z LFs and are used to investigate plausible reionization histories that are consistent with other probes of the redshift-dependent ionization degree and primarily with the electron scattering optical depth measured by the *Wilkinson Microwave Anisotropy Probe* (WMAP; Hinshaw et al. 2013).

There are also several theoretical models for the evolution of the LFs of $\text{Ly}\alpha$ emitters (LAEs) and of Lyman break galaxies (LBGs), which use different approaches. These include various semi-analytic galaxy formation models (Tilvi et al.

2009; Lo Faro et al. 2009; Kobayashi et al. 2010; Raičević et al. 2011; Garel et al. 2012; Mitra et al. 2013; Lacey et al. 2011; Gonzalez-Perez et al. 2013), smoothed particle hydrodynamics (SPH) simulations (Dayal et al. 2009, 2013; Nagamine et al. 2010; Salvaterra et al. 2011; Finlator et al. 2011b; Jaacks et al. 2012a, 2012b), and analytic models (Mao et al. 2007; Dayal et al. 2008; Samui et al. 2009; Muñoz & Loeb 2011; Muñoz 2012; Salim & Lee 2012; Tacchella et al. 2013). Each approach has known strengths and weaknesses. Given the complexity and the large number of variable parameters in many models, an analytic physical approach is particularly useful in understanding the role and the relative importance of the ingredients that come into play. We adopt such an approach, building on the work by Mao et al. (2007). As mentioned above, spectacular advances in direct determinations of the UV LFs of galaxies at epochs close to the end of reionization have recently been achieved. These imply much stronger constraints on models, particularly on the analytic ones that need to be revisited. Further constraints, generally not taken into account by all previous studies, have been provided by far-IR/(sub-)millimeter data, which probe other phases of the early galaxy evolution, concurring to delineate the complete picture.

A key novelty of the model is that it includes a self-consistent treatment of dust absorption and re-emission, which is anchored to the chemical evolution of the interstellar medium (ISM). This allows us to simultaneously account for the demography of both UV- and far-IR/(sub-)millimeter-selected high- z star-forming galaxies. In addition, the model incorporates a variety of observational constraints that are only partially taken into account by most previous studies. Specifically, we take into account constraints on: the escape fraction of ionizing photons coming from both continuum UV and Ly α line LFs and from measurements of the ratio of non-ionizing to ionizing emission from galaxies; the luminosity/stellar mass–metallicity (Maiolino et al. 2008; Mannucci et al. 2010) and the stellar mass–UV luminosity (Stark et al. 2009, 2013) relations; and the amplitude of the ionizing background at several redshifts up to $z = 6$ (Dall’Aglio et al. 2009; Wyithe & Bolton 2011; Calverley et al. 2011; Kuhlen & Faucher-Giguère 2012; Becker & Bolton 2013; Nestor et al. 2013). The successful tests of the model against a wide variety of data constitute a solid basis for extrapolations to luminosity and redshift ranges not yet directly probed by observations.

The plan of the paper is the following. In Section 2, we outline the model describing its basic ingredients. In Section 3, we exploit the model to compute the cosmic-epoch dependent UV LF, allowing for the dust extinction related to the chemical evolution of the gas. In Section 4, we compute the production rate of ionizing photons and investigate their absorption rates by both dust and neutral hydrogen (HI), as constrained by measurements of the Ly α line LFs at various redshifts and of the ratios of non-ionizing UV to Lyman-continuum luminosities. We then derive the fraction of ionizing photons that can escape into the intergalactic medium (IGM) and use the results to obtain the evolution with redshift of the volume filling factor of the intergalactic ionized hydrogen. The main conclusions are summarized in Section 5.

Throughout this paper we adopt a flat Λ CDM cosmology with matter density $\Omega_m = 0.32$, $\Omega_b = 0.049$, $\Omega_\Lambda = 0.68$; Hubble constant $h = H_0/100 \text{ km s}^{-1} \text{ Mpc}^{-1} = 0.67$; spectrum of primordial perturbations with index $n = 0.96$; and normalization $\sigma_8 = 0.83$ (Planck Collaboration 2013b). All the quoted magnitudes are in the AB system (Oke & Gunn 1983).

2. OUTLINE OF THE MODEL

In this section we present the basic features of the model used to compute the redshift-dependent UV and Lyman- α (Ly α) LFs. The model is essentially the same used by Cai et al. (2013) in his study of the evolution of the IR LF. However, the Cai et al. (2013) study dealt with a later evolutionary phase, when star formation was dust-enshrouded. Here we are interested in the phase in which dust extinction was low but growing as the gas was being enriched in metals and the dust abundance was correspondingly increasing. The associated evolution with galactic age of dust extinction is discussed in Section 2.2. In Section 2.3, the model, integrated with this additional ingredient, is tested against data on high- z galaxies not used to constrain the model parameters.

2.1. Basic Ingredients

Our approach is in line with the scenario worked out by Granato et al. (2004) and further elaborated by Lapi et al. (2006, 2011), Mao et al. (2007), and Cai et al. (2013). It exploits the outcomes of many intensive N -body simulations and semi-analytic studies (e.g., Zhao et al. 2003; Wang et al. 2011; Lapi & Cavaliere 2011) according to which pre-galactic halos undergo an early phase of fast collapse, including a few major merger events during which the central regions rapidly reach a dynamical quasi-equilibrium; a subsequent slower accretion phase follows, which mainly affects the halo outskirts. We take the transition between the two phases as the galaxy formation time.

The model envisages that during the fast collapse phase the baryons falling into the newly created potential wells are shock-heated to the virial temperature. This assumption may be at odds with analytic estimates and SPH simulations showing that the amount of shock-heated gas is relatively small for halo masses below $\sim 10^{12} M_\odot$ (Kereš et al. 2005; Dekel & Birnboim 2006), that is, in the mass range of interest here (see below). However, the analytic estimates assume spherical collapse and the SPH simulations consider a smooth initial configuration. In both cases, the results do not necessarily apply to the halo build up during the fast collapse phase, which is dominated by a few major mergers. A crucial test of the star formation history implied by the model is provided by the data discussed in the following.

An alternative picture for the formation of galaxies is the “cold stream driven” scenario, according to which massive galaxies (halo masses above $\sim 10^{12} M_\odot$) formed from steady, narrow, cold gas streams, fed by dark matter filaments from the cosmic web, that penetrate the shock-heated media of massive dark matter haloes (Dekel et al. 2009). However, this mechanism may require an implausibly high star formation efficiency (Silk & Mamon 2012; Lapi et al. 2011) and a too high bias factor of galaxies at $z \simeq 2$ (Davé et al. 2010; Xia et al. 2012). In addition, observational evidence of cold flows has been elusive. The recent adaptive optics–assisted SINFONI observations of a $z = 2.3285$ star-forming galaxy obtained at the Very Large Telescope (Bouché et al. 2013) showed evidence of cold material at about one third of the virial size of the halo. The gas appears to be co-rotating with the galaxy and may eventually inflow toward the center to feed star formation. However, this gas does not necessarily come from the intergalactic space; it may well be the result of cooling of the gas inside the halo, as implied by our scenario. In any case, as we will see in the following, massive galaxies are only of marginal importance in the present context.

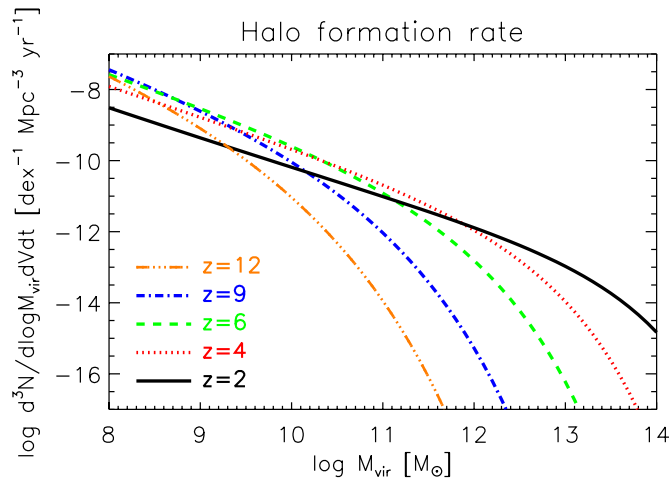


Figure 1. Evolution with redshift of the halo formation rate function. (A color version of this figure is available in the online journal.)

In our framework, the galaxy LF is directly linked to the halo formation rate, $d^3N(M_{\text{vir}}, \tau)/dM_{\text{vir}} d\tau dV$, as a function of halo mass, M_{vir} , and cosmic time, τ (see Figure 1). The halo formation rate is approximated by the positive term of the derivative with respect to τ of the cosmological halo mass function (Sasaki 1994). Lapi et al. (2013), using an excursion set approach, showed that this is a good approximation. For the halo mass function, we used the analytic approximation by Sheth & Tormen (1999).

In converting the halo formation rate into the UV LF, we also need to take into account the survival time, t_{destr} , of the halos that are subject to merging into larger halos. A short halo survival time would obviously decrease the number density of halos of given mass that are on at a given time. At the high redshifts of interest here, we expect that a large fraction of halos undergo major mergers, thus losing their individuality; therefore the survival time could impact our estimate of the LF.

The survival time is difficult to define unambiguously. We adopt the value obtained from the negative term of the time derivative, $(\partial_t N)_-$, of the Press & Schechter (1974) or of the Sheth & Tormen (1999) mass functions, that is, $t_{\text{destr}} \equiv N/(\partial_t N)_- = t_{\text{Hubble}}(z)$, independent of halo mass. In our calculations of the UV LF (Equation (9)) we cut the integration over time at t_{destr} . As we will see in the following in the mass and redshift ranges of interest here the duration of the UV bright phase of galaxy evolution is generally substantially shorter than $t_{\text{Hubble}}(z)$ and therefore also shorter than t_{destr} . Therefore, the results are only weakly affected by the cut and a more refined treatment of this tricky issue is not warranted.

The history of star formation and accretion into the central black hole (BH) were computed by numerically solving the set of equations laid down in the Appendix of Cai et al. (2013). These equations describe the evolution of the gas along the following lines. Initially, a galactic halo of mass M_{vir} contains a cosmological gas mass fraction $f_b = M_{\text{gas}}/M_{\text{vir}} = 0.17$, distributed according to a Navarro et al. (1997) density profile, with a moderate clumping factor and primordial composition. The gas is heated to the virial temperature at the virialization redshift, z_{vir} , then cools and flows toward the central regions. The cooling is fast, especially in the denser central regions where it triggers a burst of star formation. We adopt an Chabrier (2003) initial mass function (IMF). The gas cooling rate is computed by adopting the cooling function given by Sutherland & Dopita (1993). The evolution of the metal abundance of the gas is fol-

lowed using the classical equations and stellar nucleosynthesis prescriptions, as reported, for instance, in Romano et al. (2002).

An appreciable amount of cooled gas loses its angular momentum via the drag by the stellar radiation field, settles down into a reservoir around the central supermassive BH, and eventually accretes onto it by viscous dissipation, powering the nuclear activity. The supernova (SN) explosions and the nuclear activity feed energy back to the gaseous baryons, and regulate the ongoing star formation and BH growth.

The feedback from the active nucleus has a key role in quenching the star formation in very massive halos, but is only of marginal importance for the relatively low halo masses of interest here. This implies that the results presented in this paper are almost insensitive to the choice for the parameters governing the BH growth and feedback. The really important model parameters are those that regulate the star formation rate (SFR), and thus the chemical evolution. These are the clumping factor C , which affects the cooling rate; the ratio between the gas inflow timescale, t_{cond} , and the star formation timescale, t_* , $s = t_{\text{cond}}/t_*$; and the SN feedback efficiency, ϵ_{SN} .

For the first two of the latter parameters, clumping factor C and ratio s ,—as well as for all the parameters controlling the growth of and the feedback from the active nucleus that, albeit almost irrelevant, are nevertheless included in our calculations—we adopt the values determined by Lapi et al. (2006) and also used by Lapi et al. (2011) and Cai et al. (2013) (i.e., $C = 7$ and $s = 5$). A discussion on the plausible ranges for all the model parameters can be found in Cai et al. (2013).

However, we have made a different choice for ϵ_{SN} , which is motivated by the fact that the earlier papers dealt with relatively high halo masses ($M_{\text{vir}} \gtrsim 10^{11.2} M_{\odot}$) whereas, at the high redshifts of interest here, the masses of interest are substantially lower. As pointed out by Shankar et al. (2006), the data indicate that the star formation efficiency in low-mass halos must be lower than implied by the SN feedback efficiency gauged for higher halo masses. In other words, as extensively discussed in the literature, external (UV background) or internal (SN explosions, radiation from massive low-metallicity stars, and, possibly, stellar winds) heating processes can reduce the SFR in low-mass halos (e.g., Pawlik & Schaye 2009; Hambrick et al. 2011; Finlator et al. 2011a; Krumholz & Dekel 2012; Pawlik et al. 2013; Wyithe & Loeb 2013; Sobacchi & Mesinger 2013) and completely suppress it below a critical halo mass, M_{crit} .

We take this into account by increasing the SN feedback efficiency with decreasing halo mass and introducing a low-mass cutoff (i.e., considering only galaxies with $M_{\text{vir}} \geq M_{\text{crit}}$). We set

$$\epsilon_{\text{SN}} = 0.05\{3 + \text{erf}[-\log(M_{\text{vir}}/10^{11} M_{\odot})/0.5]\}/2, \quad (1)$$

which converges, for $M_{\text{vir}} > 10^{11} M_{\odot}$, to the constant value, $\epsilon_{\text{SN}} = 0.05$, used by Cai et al. (2013).

The critical halo mass can be estimated by equating the gas thermal speed in virialized halos to the escape velocity to find $M_{\text{crit}} \simeq 2 \times 10^8 (T/2 \times 10^4 \text{ K})^{3/2} M_{\odot}$ (Hambrick et al. 2011), where $2 \times 10^4 \text{ K}$ corresponds to the peak of the hydrogen cooling curve. If the balance between heating and cooling processes results in higher gas temperatures, M_{crit} can increase even by a large factor. An accurate modeling of the physical processes involved is difficult and numerical simulations yield estimates of $M_{\text{crit}}/M_{\odot}$ in the range from 4×10^8 to $\gtrsim 10^9$ (Hambrick et al. 2011; Krumholz & Dekel 2012; Pawlik et al. 2013; Sobacchi & Mesinger 2013), with a trend toward lower values at $z > 6$ when the IGM was cooler (e.g., Dijkstra et al. 2004; Kravtsov

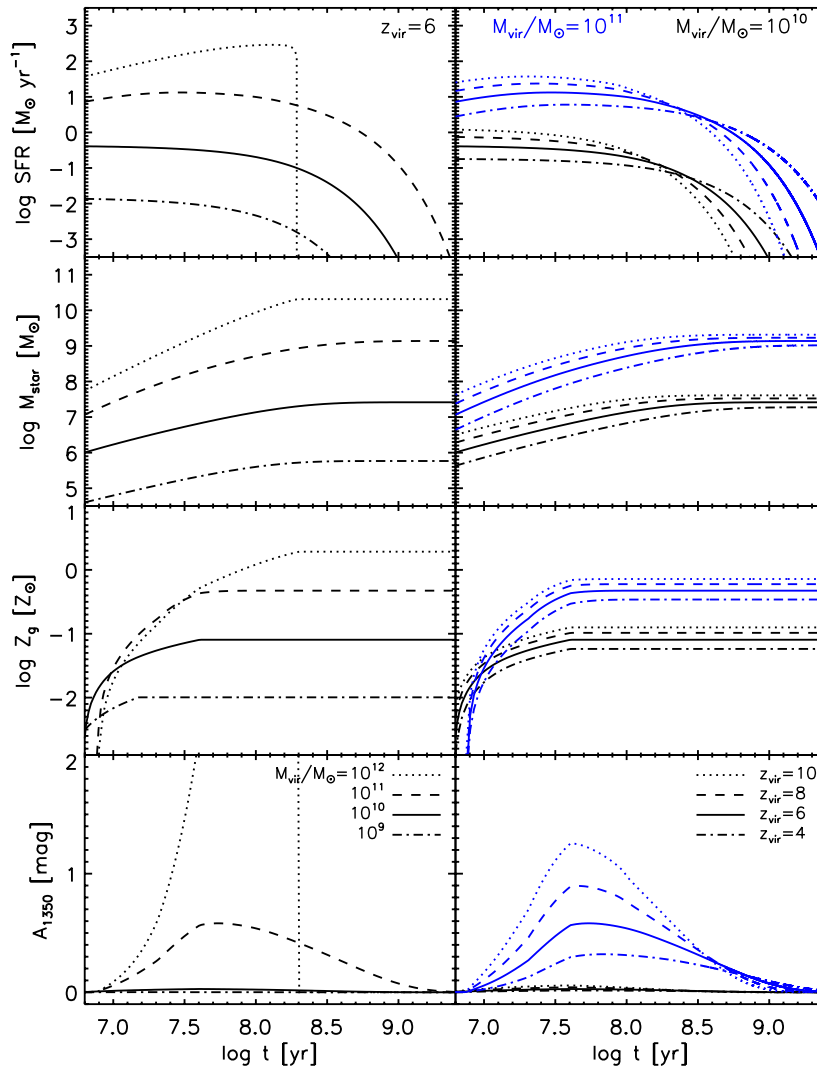


Figure 2. Left panels: evolution with galactic age of the SFR; the stellar mass, M_{star} ; the gas metallicity, Z_g ; and the dust extinction, A_{1350} (from top to bottom) for halo masses of $M_{\text{vir}} = 10^9$ (dot-dashed lines), 10^{10} (solid lines), 10^{11} (dashed lines), and $10^{12} M_{\odot}$ (dotted lines) virialized at $z_{\text{vir}} = 6$. The galactic age is measured from the virialization redshift (i.e., $t = 0$ for $z = z_{\text{vir}}$). Right panels: evolution of the quantities on the left panels at the fixed halo mass ($M_{\text{vir}} = 10^{10}$ and $10^{11} M_{\odot}$, black and blue lines, respectively) for different redshifts: $z_{\text{vir}} = 4$ (dot-dashed lines), 6 (solid lines), 8 (dashed lines), and 10 (dotted lines).

(A color version of this figure is available in the online journal.)

et al. 2004; Okamoto et al. 2008) and the intensity of the UV background is expected to decrease.

If, on one side, heating properties can decrease the SFR in small galactic halos, the production of UV photons per unit stellar mass is expected to substantially increase with redshift, at least at $z \gtrsim 3$. Padoan et al. (1997) argued that the characteristic stellar mass, corresponding to the peak in the IMF per unit logarithmic mass interval, scales as the square of the temperature, T_{mc} , of the giant molecular clouds within which stars form. But the typical local value of T_{mc} (~ 10 K) is lower than the cosmic microwave background (CMB) temperature at $z \gtrsim 3$ implying a rapid increase with z of the characteristic stellar mass, and thus of the fraction of massive stars producing UV photons. On the other hand, a higher fraction of massive stars also implies a more efficient gas heating, which leads to a stronger quenching of the SFR. This complex set of phenomena tends to counterbalance each other. Therefore, in the following we adopt, above M_{crit} , the SFR given by the model and the UV (ionizing and non-ionizing) photon production rate appropriate to the Chabrier (2003) IMF, allowing for the possibility of a correction factor to be determined by comparison with the data.

2.2. Evolution of Galaxy Properties

The model outlined above allows us to compute the evolution with galactic age of the SFR; the mass in stars; the metal abundance of the gas as a function of the halo mass, M_{vir} ; and the halo virialization redshift, z_{vir} . Examples illustrating four values of the halo mass at fixed $z_{\text{vir}} = 6$ (left panels) and for four values of z_{vir} and two values of the halo mass (right panels) are shown in Figure 2. A few points are worth noting. (1) The active star formation phase in the most massive halos ($M_{\text{vir}} \gtrsim 10^{12} M_{\odot}$) is abruptly terminated by the active galactic nucleus (AGN) feedback, while in less massive halos, where the feedback is dominated by stellar processes, the SFR declines more gently; (2) at fixed halo mass the SFR is initially higher at higher redshifts (mainly because the higher densities imply faster cooling of the gas) and declines earlier; (3) the higher star formation efficiency at higher z implies that the stellar to halo mass ratio and the metallicity are higher for galaxies that formed at higher redshifts. The different behavior of these quantities for different halo masses and different redshifts determines the relative contributions of the various masses to

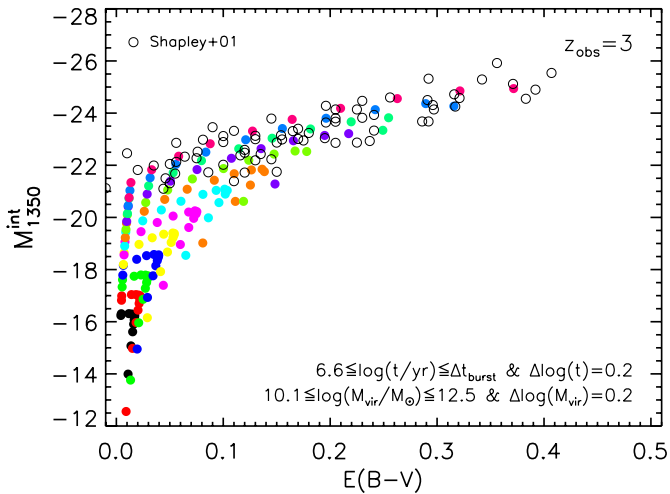


Figure 3. Correlation of the intrinsic (extinction-corrected) rest-frame absolute UV magnitude, M_{1350}^{int} , with the color excess, $E(B-V)$. The open circles are the data by Shapley et al. (2001, see their Figure 11) corrected for the different cosmology used here, the filled circles show the expectations of our model using the extinction law of Equation (2) for halo masses in the range $10^{10} M_{\odot} \lesssim M_{\text{vir}} \lesssim 4 \times 10^{12} M_{\odot}$ sampled in intervals $\Delta \log M_{\text{vir}} = 0.2$, and for ages in the range $4 \times 10^6 \lesssim t/\text{yr} \lesssim \Delta t_{\text{burst}}(M_{\text{vir}}, z_{\text{obs}})$ (see Appendix of Fan et al. 2010 for an approximation of the duration of the star formation phase, Δt_{burst} , as a function of halo mass and redshift). The relation $E(B-V) \approx A_{1350}/11$ by Calzetti et al. (2000) has been adopted.

(A color version of this figure is available in the online journal.)

the LFs and their evolution with cosmic time, as discussed in the following.

For comparisons with the data we further need to take into account the dust extinction, which is proportional to the dust column density. In turn, the dust column density is proportional to the gas column density, N_{gas} , times the metallicity, Z_{g} , to some power reflecting the fraction of metals locked into dust grains. We thus expect that at our reference UV wavelength, 1350 Å, the dust extinction is $A_{1350} \propto \dot{M}_{\star}^{\alpha} Z_{\text{g}}^{\beta}$, where \dot{M}_{\star}^{α} is the star formation rate. Mao et al. (2007) found that a relationship of this kind ($A_{1350} \approx 0.35 (\dot{M}_{\star}/M_{\odot} \text{yr}^{-1})^{0.45} (Z_{\text{g}}/Z_{\odot})^{0.8}$) does indeed provide a good fit for the luminosity–reddening relation found by Shapley et al. (2001). We have adopted a somewhat

different relation

$$A_{1350} \approx 0.75 \left(\frac{\dot{M}_{\star}}{M_{\odot} \text{yr}^{-1}} \right)^{0.25} \left(\frac{Z_{\text{g}}}{Z_{\odot}} \right)^{0.3}, \quad (2)$$

which we have found provides a better fit for the UV LFs of LBGs (Reddy & Steidel 2009; Bouwens et al. 2007; McLure et al. 2013, see below) while still being fully consistent with the Shapley et al. (2001) data (see Figure 3), as well as with observational estimates of the escape fractions ($f_{\lambda}^{\text{esc}} = \exp(-A_{\lambda}/1.08)$, see below) of UV and Ly α photons (Figure 4).

As illustrated by the bottom left panel of Figure 2, the UV extinction is always low for the least massive galaxies ($M_{\text{vir}} \lesssim 10^{11} M_{\odot}$), but increases rapidly with increasing M_{vir} . This implies a strong correlation between dust attenuation and halo/stellar mass, thus providing a physical explanation for the correlation reported by Heinis et al. (2014, see their Figure 3). The bottom right panel of the figure shows that at fixed halo/stellar mass the model implies a mild increase of the attenuation with increasing z , paralleling the small increase in the gas metallicity due to the higher star formation efficiency.

The observed absolute magnitude in the AB system of a galaxy at our reference UV wavelength, $\lambda = 1350$ Å, is related to its SFR and to dust extinction A_{λ} as

$$M_{1350}^{\text{obs}} = 51.59 - 2.5 \log \frac{L_{1350}^{\text{int}}}{\text{erg s}^{-1} \text{Hz}^{-1}} + A_{1350}, \quad (3)$$

with

$$L_{1350}^{\text{int}} = k_{\text{UV}} \dot{M}_{\star}, \quad (4)$$

where L_{1350}^{int} is the intrinsic monochromatic luminosity at the frequency corresponding to 1350 Å. On account of the uncertainties on the IMF at high z , mentioned above, we treat the normalization factor k_{UV} ($\text{erg s}^{-1} \text{Hz}^{-1} M_{\odot}^{-1} \text{yr}$) as an adjustable parameter. Using the evolutionary stellar models of Fagotto et al. (1994a, 1994b), we find that k_{UV} varies with galactic age and gas metallicity as illustrated by Figure 5. The main contributions to the UV LF come from galactic ages $\gtrsim 10^7$ yr, when $\log(k_{\text{UV}}) \gtrsim 27.8$, and is somewhat higher for lower metallicity. We adopt $\log(k_{\text{UV}}) = 28$ as our reference value. We note that the relationship between the absolute AB magnitude at the effective frequency ν , M_{ν} , and the luminosity is

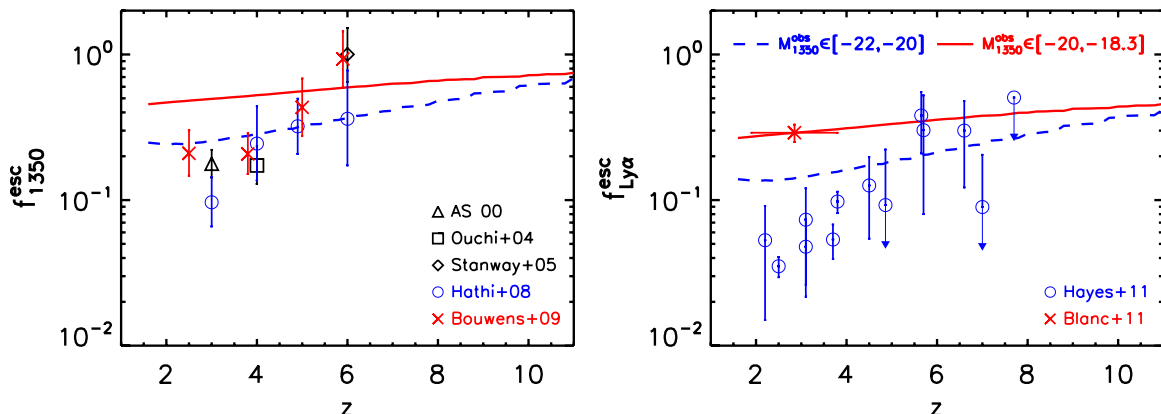


Figure 4. Average escape fractions of UV (f_{1350}^{esc} , left panel) and Ly α photons ($f_{\text{Ly}\alpha}^{\text{esc}}$, right panel) given by the model as a function of redshift, compared with observational estimates by Adelberger & Steidel (2000, AS 00), Ouchi et al. (2004), Stanway et al. (2005), Hathi et al. (2008), Bouwens et al. (2009), Blanc et al. (2011), and Hayes et al. (2011) for two bins of observed UV magnitudes: $M_{1350}^{\text{obs}} \in [-22, -20]$ (blue dashed line and data points) and $M_{1350}^{\text{obs}} \in [-20, -18.3]$ (red solid line and data points), roughly corresponding to LBGs and LAEs, respectively.

(A color version of this figure is available in the online journal.)

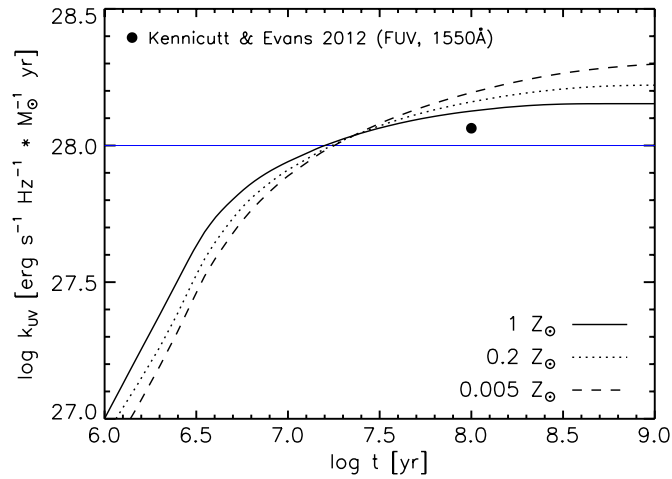


Figure 5. Evolution with galactic age of the coefficient k_{UV} (Equation (4)) for a constant SFR, a Chabrier (2003) IMF, and three gas metallicities: $Z_g = 0.005$ (dashed line), 0.02 (dotted line), and $1 Z_\odot$ (solid line). The far-UV/SFR calibration by Kennicutt & Evans (2012) for solar metallicity and a Kroupa IMF is also shown (filled circle at $\log(t/\text{yr}) = 8$). The horizontal blue line corresponds to the value adopted in the present paper.

(A color version of this figure is available in the online journal.)

$$\log[(\nu L_\nu)/L_\odot] = 2.3995 - \log(\lambda/1350 \text{ \AA}) - 0.4 M_\nu, \text{ where } L_\odot = 3.845 \times 10^{33} \text{ erg s}^{-1}.$$

We adopt the standard “dust screen” model for dust extinction, so that the observed luminosity is related to the intrinsic one by

$$L^\text{obs}(\lambda) = L^\text{int}(\lambda)10^{-0.4A_\lambda}, \quad (5)$$

with the Calzetti et al. (2000) reddening curve holding for $0.12 \mu\text{m} \leq \lambda \leq 0.63 \mu\text{m}$,

$$A_\lambda/E_s(B-V) \simeq 2.659(-2.156 + 1.509/\lambda - 0.198/\lambda^2 + 0.011/\lambda^3) + R_V, \quad (6)$$

where $E_s(B-V)$ is the color excess of the galaxy stellar continuum and $R_V = 4.05$. This gives $A_{1350}/E_s(B-V) \simeq 11.0$ and $A_{1216} \simeq 1.08A_{1350}$. Oesch et al. (2013c) found that the dust reddening at $z \simeq 4$ is better described by a Small Magellanic Cloud (SMC) extinction curve (Pei 1992) rather than by the Calzetti curve. However, for our purposes the only relevant quantity is the A_{1216}/A_{1350} ratio. Using the Pei (1992) fitting function for the SMC curve, we find $(A_{1216}/A_{1350})_{\text{SMC}} = 1.14$, which is very close to the Calzetti ratio (1.08). Thus our results would not appreciably change adopting the SMC law.

2.3. Testing the Model Against High- z Data

Some average properties, which are weighted by the halo formation rate, of galaxies at $z_{\text{obs}} = 2, 6,$ and 12 are shown as a function of the observed luminosity in Figures 6 and 7. The weighted averages have been computed as follows. We sample the formation rate of halos with mass M_{vir} virializing at t_{vir} , $\dot{n}(M_{\text{vir}}, t_{\text{vir}}) \equiv d^3 N(M_{\text{vir}}, t_{\text{vir}})/d \log M_{\text{vir}} dt dV$, in steps of $\Delta \log M_{\text{vir}} = 0.08$ and cosmic time interval $\Delta t_{\text{vir}} = 4$ Myr, and select those having some property X , like the UV, L_{1350} , luminosity; the Ly α , L_{1216} , luminosity; or the stellar mass (actually we set $X = \log(\text{quantity})$) in a given range, $X_i \in (X - \Delta X/2, X + \Delta X/2)$, at the selected z_{obs} . The average value, $\mu_Y(X, \Delta X)$, of some other property Y (e.g., age of stellar populations, t_{age} , gas metallicity, Z_g , SFR, etc.) is

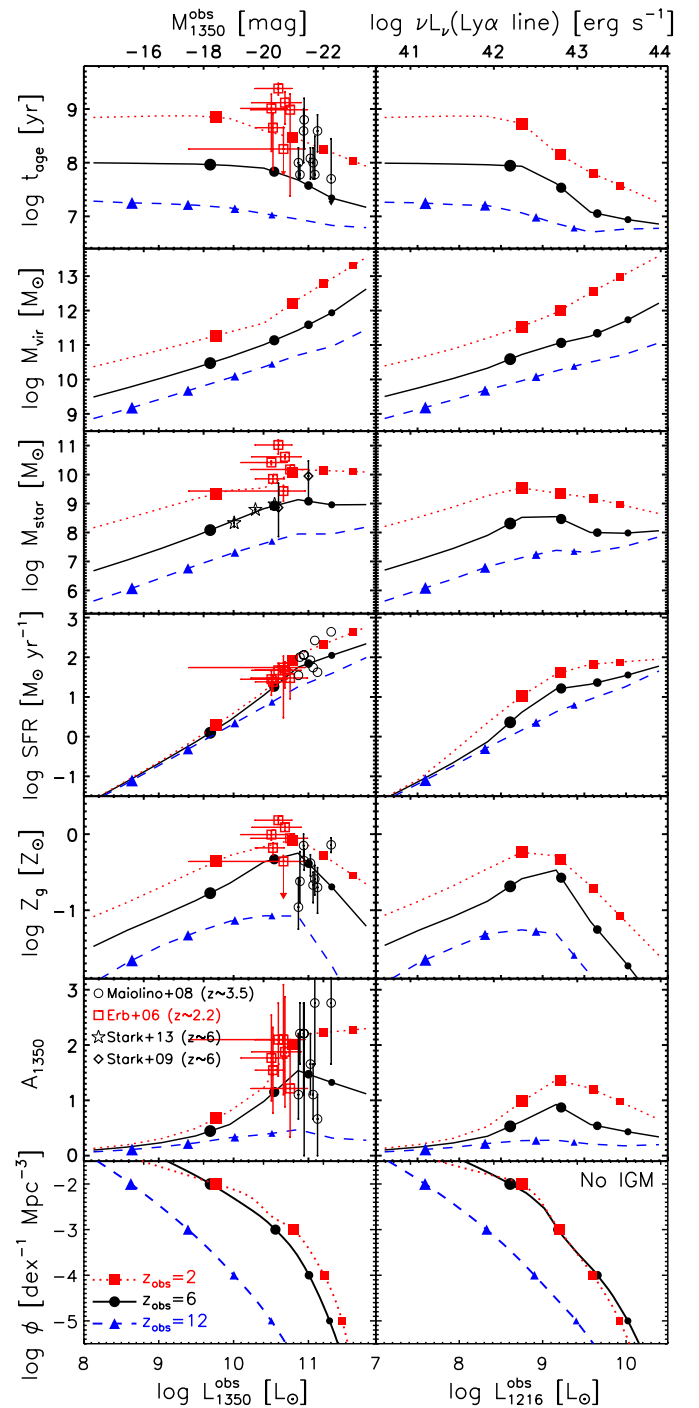


Figure 6. Average properties, weighted by the halo formation rate, of model galaxies at $z_{\text{obs}} = 2, 6,$ and 12 (dotted red lines and filled red squares, solid black line and black circles, and dashed blue line and blue triangles, respectively) as a function of the observed UV luminosity (left panels) and of the observed Ly α line luminosity without the IGM attenuation (right panels). Larger symbols correspond to more numerous objects: the comoving number densities at the bin centers are $10^{-5}, 10^{-4}, 10^{-3},$ and $10^{-2} \text{ dex}^{-1} \text{ Mpc}^{-3}$, respectively; the bottom panels show the corresponding luminosities. Points with error bars show observational estimates. The red open squares show the mean properties of 87 LBGs at $z \sim 2.2$ (Erb et al. 2006), and the black open circles show those for 9 LBGs at $z \sim 3.5$ (Maiolino et al. 2008). The stellar mass–luminosity relation at $z \sim 6$ given by Stark et al. (2009) and Stark et al. (2013; broadband fluxes corrected for possible contamination of nebular emission) are also shown. The legend for data symbols, given in the left A_{1350} panel, applies to the data in all panels.

(A color version of this figure is available in the online journal.)

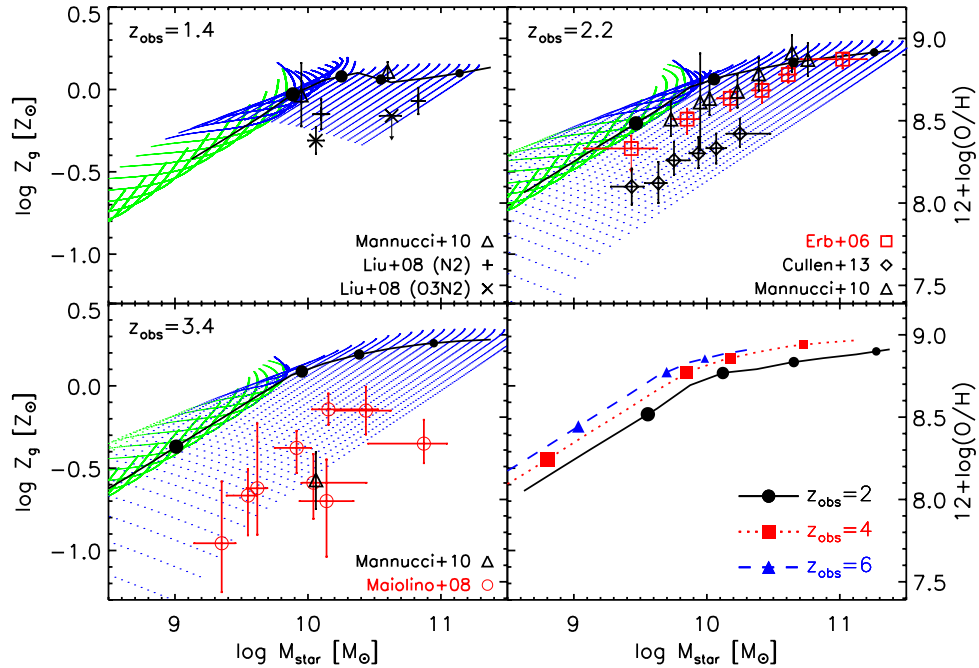


Figure 7. Gas metallicity versus stellar mass at various redshifts, specified in the upper left corner of each panel. The green and blue dotted lines refer to model galaxies with halo masses of $10.5 \lesssim \log(M_{\text{vir}}/M_{\odot}) \lesssim 11.5$ and $11.5 \lesssim \log(M_{\text{vir}}/M_{\odot}) \lesssim 13.3$, respectively. The limited extent of the blue dotted lines at $z = 1.4$ follows from the adopted lower limit to the considered virialization redshifts ($z_{\text{vir}} \geq 1.5$), which translates into a lower limit to the stellar mass in massive halos at this redshift. The black solid lines show the average mass–metallicity relation for model galaxies, which are weighted by the halo formation rate. The black filled circles correspond to comoving number densities decreasing from 10^{-2} to $10^{-5} \text{ dex}^{-1} \text{ Mpc}^{-3}$ in steps of one dex, with symbol size decreasing with the number density. The bottom right panel shows the evolution of the gas metallicity versus stellar mass relation from $z_{\text{obs}} = 2$ to $z_{\text{obs}} = 6$. The data points are (see the legend within each panel) from Erb et al. (2006), Liu et al. (2008), Maiolino et al. (2008), Mannucci et al. (2010), and Cullen et al. (2013).

(A color version of this figure is available in the online journal.)

then computed as

$$\mu_Y(X, \Delta X) = \frac{\sum_i Y_i \dot{n}_i \theta_H(X - \Delta X/2 < X_i \leq X + \Delta X/2)}{\sum_i \dot{n}_i \theta_H(X - \Delta X/2 < X_i \leq X + \Delta X/2)}, \quad (7)$$

where θ_H ($\theta_H(x) = 1$ if x is true, $\theta_H(x) = 0$ otherwise) is the Heaviside function. The comoving number density of galaxies satisfying the selection criterion is

$$n(X, \Delta X) = \frac{1}{\Delta X} \sum_i \dot{n}_i \cdot \Delta \log M_{\text{vir}} \cdot \Delta t_{\text{vir}} \cdot \theta_H(X - \Delta X/2 < X_i \leq X + \Delta X/2). \quad (8)$$

The data we compare with are specified in the panels and in the captions of the figures. Note that these data were *not* used to constrain the model parameters. As illustrated by Figure 6, the model compares favorably with observational estimates of various galaxy properties at different redshifts. Stellar population ages are, on average, substantially younger for the brighter galaxies, which are associated with the most massive halos. This is fully consistent with the well established “downsizing” scenario, since it happens because massive galaxies have high SFRs that may reach $\text{SFR} \sim 100 M_{\odot} \text{ yr}^{-1}$ and therefore develop their stellar populations faster. The chemical enrichment and the associated dust obscuration also grow faster in these galaxies that soon become UV-faint. This causes a downward trend of t_{age} with increasing L_{1350}^{obs} , which is consistent with the data (upper left panel of Figure 6).

To compare the predictions of our model with observations on the metallicity–luminosity and metallicity–stellar mass relations at different redshifts, we have converted the values of

$[12 + \log(\text{O}/\text{H})]$ given by Maiolino et al. (2008) and Liu et al. (2008) to Z_g in solar units adopting a solar oxygen abundance $[12 + \log(\text{O}/\text{H})]_{\odot} = 8.69$ (Asplund et al. 2009). In Figure 7 the stellar masses estimated by Maiolino et al. (2008) assuming a Salpeter IMF have been divided by a factor of 1.4 to convert them to the Chabrier IMF used in the model. We have also plotted the metallicity estimates by Erb et al. (2006) for a sample of 87 LBGs at $z \sim 2.2$, as revised by Maiolino et al. (2008) using an improved calibration. Cullen et al. (2013) found an offset in the relation for $z \sim 2$ galaxies compared to Erb et al. (2006). They argue that the difference originates from the use of different metallicity estimators with locally calibrated metallicity relations that may not be appropriate for the different physical conditions of star-forming regions at high redshifts.

The dependence of gas-phase metallicity on stellar mass, with lower M_{\star} galaxies having lower metallicities, is accounted for by the model, at least at $z_{\text{obs}} = 2.2$ (Figure 7). This trend is also present in the data on $z_{\text{obs}} = 3.4$ galaxies by Maiolino et al. (2008), which indicate a decrease by 0.6 dex of the amplitude of the Z_g – M_{\star} relation compared to that observed at $z_{\text{obs}} = 2.2$. Such a strong evolution is at odds with model predictions, according to which the evolution should be quite weak, as shown in the bottom right panel of Figure 7. However, as argued by Cullen et al. (2013), the strong evolution may be an artifact due to the use of locally calibrated metallicity indicators, which do not account for evolution in the physical conditions of star-forming regions.

3. THE REDSHIFT-DEPENDENT UV LUMINOSITY FUNCTION

In the previous section we introduced all the ingredients needed to compute the population properties of high- z galaxies.

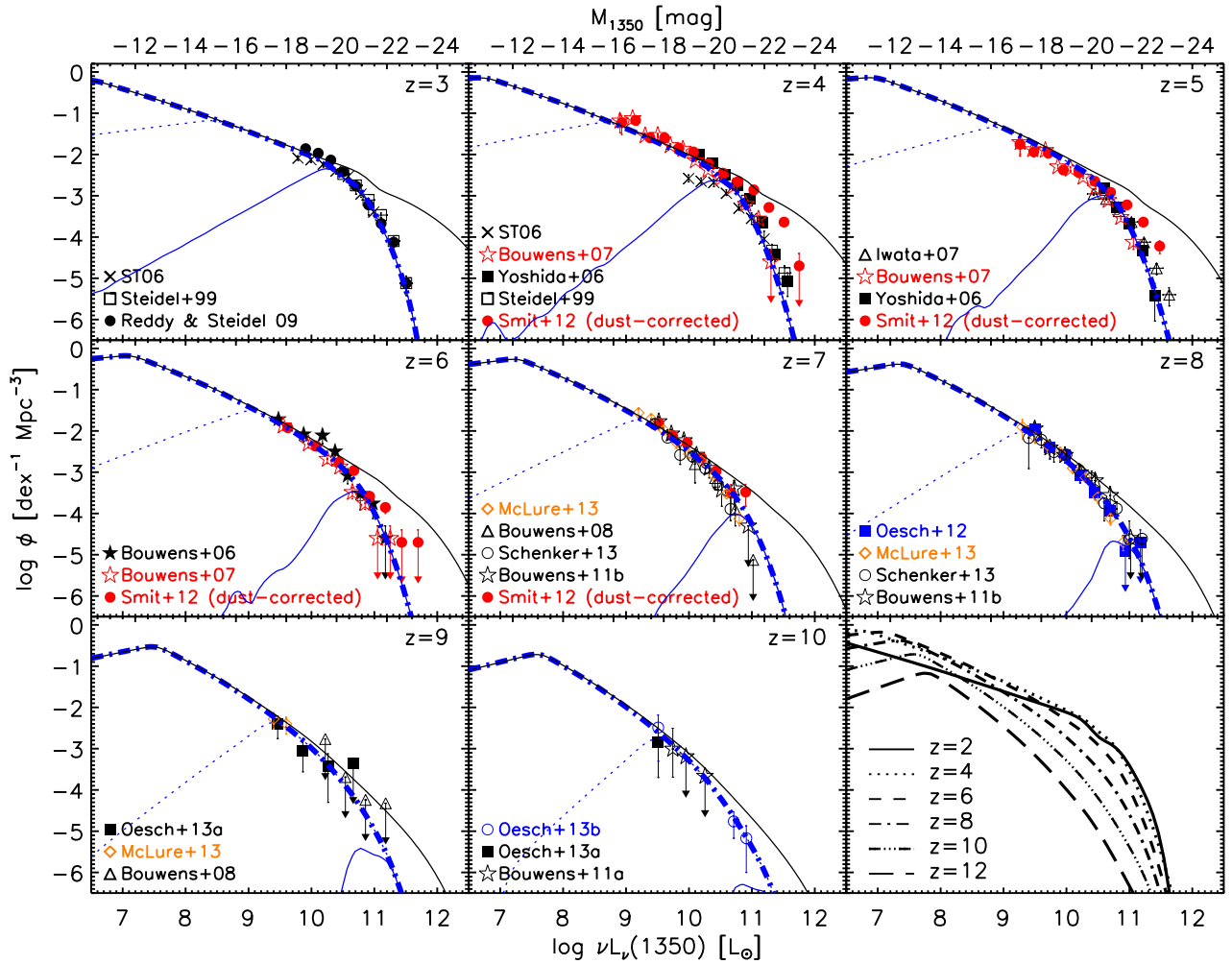


Figure 8. Luminosity functions at 1350 Å at several redshifts, specified in the upper right corner of each panel. The upper scale gives the UV magnitudes corresponding to the UV luminosities at 1350 Å. The solid black lines show the predicted luminosity function neglecting extinction, whereas the dot-dashed blue lines include the effect of extinction. The low luminosity break corresponds to $M_{\text{crit}} = 10^{8.5} M_{\odot}$. The thin dotted and solid blue lines show the effect of increasing the minimum halo mass to $10^{9.8}$ and $10^{11.2} M_{\odot}$, respectively, including extinction. The extinction mostly affects the highest luminosities, which are associated to the most massive objects that have the fastest chemical enrichment (see Figure 2). As illustrated by the bottom right panel, which shows the evolution of the luminosity function, its faint portion is predicted to steepen with increasing redshift. The model implies a weak evolution of the luminosity function from $z = 2$ to $z = 6$. The data are from Steidel et al. (1999), Sawicki & Thompson (2006a, ST06), Yoshida et al. (2006), Iwata et al. (2007), Reddy & Steidel (2009, RS09), Bouwens et al. (2006, 2007, 2008, 2011a, 2011b), Smit et al. (2012), Schenker et al. (2013), McLure et al. (2013), and Oesch et al. (2012, 2013a, 2013b). Only the estimates by Smit et al. (2012) include an (uncertain) correction for dust extinction, based on the slope of the UV continuum.

(A color version of this figure is available in the online journal.)

We now proceed with the calculation of the cosmic epoch-dependent UV LF and discuss the role of dust extinction in shaping it (Section 3.1); the constraints on its faint end (Section 3.2) that, as we shall see, are important in the context of understanding the cosmic reionization and its cosmological evolution (Section 3.3); and the transition from the dust-free to the dust-enshrouded star formation phases (Section 3.4).

The comoving differential UV LF $\Phi(\log L_{1350}^{\text{obs}}, z)$ (i.e., the number density of galaxies per unit $\log L_{1350}^{\text{obs}}$ interval at redshift z) can be computed by coupling the halo formation rate with the relationship between halo mass and SFR as a function of cosmic time, τ , and with the relationship between SFR and UV luminosity (Equation (3)) to obtain

$$\Phi(\log L_{1350}^{\text{obs}}, z) = \int_{M_{\text{vir}}^{\text{min}}}^{M_{\text{vir}}^{\text{max}}} dM_{\text{vir}} \int_z^{z_{\text{vir}}^{\text{max}}} dz_{\text{vir}} \left| \frac{d\tau_{\text{vir}}}{dz_{\text{vir}}} \right| \times \frac{d^3 N}{dM_{\text{vir}} d\tau_{\text{vir}} dV} \theta_{\text{H}}[t(z) - t(z_{\text{vir}}) < t_{\text{destr}}(z_{\text{vir}})], \quad (9)$$

where L_{1350}^{obs} is the observed luminosity, attenuated by dust, and $\theta_{\text{H}}(x)$ is the Heaviside function. We set $z_{\text{vir}}^{\text{max}} = 16$, $M_{\text{vir}}^{\text{max}} = 10^{13.3} M_{\odot}$, and $M_{\text{vir}}^{\text{min}} = M_{\text{crit}}$.

Figure 8 shows that the model is nicely consistent with observational estimates of the UV LF over the full redshift range from $z \sim 3$ to $z \sim 10$ for $k_{\text{UV}} = 1.0 \times 10^{28} \text{ erg s}^{-1} \text{ Hz}^{-1} M_{\odot}^{-1} \text{ yr}$ (Equation (4), see also Figure 5). Observational determinations of UV LFs were made at various rest-frame wavelengths. However, because the UV continuum slope, β ($f_{\lambda} \propto \lambda^{\beta}$), of high- z galaxies is close to $\beta = -2$ (Bouwens et al. 2012; Castellano et al. 2012), the color correction $M_{\text{AB},\lambda_1} - M_{\text{AB},\lambda_2} = -2.5(\beta + 2) \log(\lambda_1/\lambda_2)$ is small and has been neglected.

3.1. The Role of Dust Extinction

Dust extinction is differential in luminosity as is clearly seen by comparing the solid black lines (no extinction) in Figure 8 with the dot-dashed blue lines (extinction included). This follows from the faster metal enrichment in the more

massive objects (see Figure 2), where the SN and radiative feedbacks are less effective in depressing the SFR.

Figure 2 also shows that the least massive galaxies ($M_{\text{vir}} < 10^{11} M_{\odot}$) have low extinction throughout their lifetime. In conjunction with the fast decline of the number density of more massive halos, this results in an increasing dominance of the contribution of low mass galaxies to the UV LF at higher and higher z . Figure 8 indeed shows that the observed portion of the UV LF at $z \geq 7$ is accounted for by galaxies with $M_{\text{vir}} < 10^{11.2} M_{\odot}$, and the effect of dust extinction is negligible over most of the observed luminosity range. This offers the interesting possibility of reconstructing the halo formation rate from the UV LF without the complication of uncertain extinction corrections.

3.2. The Faint End of the UV Luminosity Function

At the faint end the LF has a break corresponding to M_{crit} , the mass below which the star formation is suppressed by external and internal heating processes (see Section 2). In Figure 8 $M_{\text{crit}} = 10^{8.5} M_{\odot}$, but in the panels comparing the model with the data at various redshifts the thin dotted and solid blue lines show the effect of increasing M_{crit} to $10^{9.8} M_{\odot}$ and $10^{11.2} M_{\odot}$, respectively. This shows that the data only constrain M_{crit} to be $\lesssim 10^{9.8} M_{\odot}$, which is consistent with estimates from simulations as summarized in Section 2.1.

Interestingly, Muñoz & Loeb (2011), using a substantially different model, find that the observed UV LFs at $z = 6, 7,$ and 8 are best fit with a minimum halo mass per galaxy $\log(M_{\text{min}}/M_{\odot}) = 9.4(+0.3, -0.9)$ in good agreement with our estimate. Whereas these authors simply assume negligible dust extinction at these redshifts, our model provides a quantitative physical account of the validity of this assumption. Raičević et al. (2011), using the Durham GALFORM semi-analytical galaxy formation model, also find that the minimum halo mass that substantially contributes to the production of UV photons at these redshifts is $\log(M_{\text{min}}/h^{-1} M_{\odot}) \simeq 9$. A lower value, $\log(M_{\text{min}}/M_{\odot}) \simeq 8.2$, was obtained by Jaacks et al. (2012a) from their cosmological hydrodynamical simulations. Trenti et al. (2010) derive from abundance matching that the galaxies currently detected by *HST* live in dark matter halos with $M_H \gtrsim 10^{10} M_{\odot}$, and they predict a weak decrease of the star formation efficiency with decreasing halo mass down to a minimum halo mass for star formation $M_H \sim 10^8 M_{\odot}$, under the assumption that the luminosity function remains a steep power law at the faint end.

The higher feedback efficiency for less massive halos (Equation (1)) makes the slope of the faint end of the UV LF (above the break) flatter than that of the low mass end of the halo formation rate function (as illustrated by Figure 1). However, the former slope reflects to some extent the steepening with increasing redshift of the latter. Just above the low-luminosity break corresponding to M_{crit} , the slope $-d \log \Phi(L_{1350}^{\text{obs}}, z)/d \log L_{1350}^{\text{obs}}$ (where Φ is per unit $d \log L_{1350}^{\text{obs}}$) steadily increases from $\simeq 0.5$ at $z = 2$ to $\simeq 0.7$ at $z = 6$ and $\simeq 1$ at $z = 10$ (see the bottom right panel of Figure 8). The steepening of the faint end of the UV LF with increasing z implies an increasing contribution of low luminosity galaxies to the UV background. The dust extinction, differential with halo mass, further steepens the bright end of the observed UV LF.

3.3. Evolution of the UV Luminosity Function

As shown by the bottom right panel of Figure 8, the model implies that the evolution of the UV LF from $z = 2$ to $z = 6$ is

weak. In particular the fast decrease with increasing redshift of the high mass halo formation rate (Figure 1) is not mirrored by the bright end of the LF. This is partly due, again, to the fast metal enrichment of massive galaxies, which translates into a rapid increase of dust extinction and, consequently, in a short duration of their UV bright phase (Figure 2). Thus the contribution to the UV LF of galaxies in halos more massive than $\sim 10^{11.2} M_{\odot}$ (thin, solid blue line in Figure 8) decreases rapidly with increasing redshift and galaxies with $M_{\text{vir}} \gg 10^{11.2} M_{\odot}$ contribute very little. The UV LF at high z is therefore weakly sensitive to the rapid variation of the formation rate of the latter galaxies. The milder decrease of the formation rates of less massive galaxies is largely compensated by the increase of the star formation efficiency due to the faster gas cooling (see Figure 2). At $z > 6$, however, the decrease of the formation rate even of intermediate mass galaxies prevails and determines a clear negative evolution of the UV LF.

3.4. From Dust-free to Dust-enshrouded Star Formation

As illustrated by the bottom left panel of Figure 2, the star formation in massive galaxies is dust enshrouded over most of its duration. For example, the figure shows that the extinction at 1350 \AA of a galaxy with $M_{\text{vir}} = 10^{12} M_{\odot}$ is already growing at galactic ages of a few times 10^7 yr, reaching two magnitudes at an age of 4×10^7 yr. The total duration of the star formation phase for these galaxies is $\simeq 7 \times 10^8 [(1+z)/3.5]^{-1.5}$ yr (Cai et al. 2013), which implies that they show up primarily at far-IR/(sub-)millimeter wavelengths. Thus the present framework entails a continuity between the high- z galaxy SFR function derived from the UV LF (dominated by low-mass galaxies) and that derived from the infrared (IR; 8–1000 μm) LF (dominated by massive galaxies), investigated by Lapi et al. (2011) and Cai et al. (2013). This continuity is borne out by observational data at $z = 2$ and 3 , as shown by Figure 9. Once proper allowance for the effect of dust attenuation is made, the model accurately matches the IR and the UV LFs and, as expected, UV and IR data cover complementary SFR ranges.

The SFR histories inferred from UV and far-IR data are compared in Figure 10 (see also Fardal et al. 2007). This figure shows that the ratio of dust-obscured to unobscured SFR increases with increasing redshift until it reaches a broad maximum at $z \sim 2$ – 3 and decreases afterward. This entails a prediction for the evolution of the IR luminosity density, ρ_{IR} , beyond $z \simeq 3.5$, where it cannot yet be determined observationally. At these redshifts, according to the present model, ρ_{IR} decreases with increasing z faster than the UV luminosity density, ρ_{UV} . In other words, the extinction correction needed to determine the SFR density from the observed ρ_{UV} is increasingly small at higher and higher redshifts. This is because the massive halos that can reach high values of dust extinction become increasingly rare at high z .

4. IONIZING PHOTONS

We now move from the non-ionizing to the ionizing UV. Two issues need to be addressed: the production rate of ionizing photons as a function of halo mass and galactic age, and the fraction that manages to escape into the IGM, thus contributing to the ionization rate. Key information on both issues is provided by the Ly α line LF, which is observationally determined up to $z \simeq 8$ and with some constraints also at $z \simeq 9$. As discussed in Section 4.1, the observed Ly α luminosity of a galaxy is directly proportional to the production rate of ionizing photons, their absorption fraction by H I in the ISM, and the

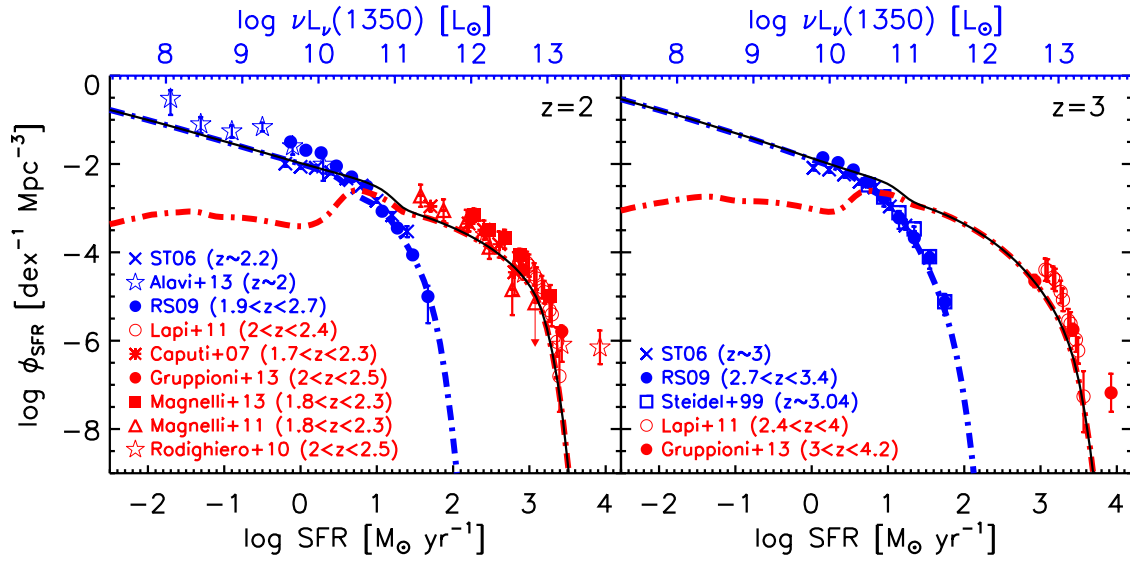


Figure 9. Comparison of the SFR functions yielded by the model at $z = 2$ and 3 with those inferred from IR ($8\text{--}1000\ \mu\text{m}$, red data points Caputi et al. 2007; Rodighiero et al. 2010; Lapi et al. 2011; Gruppioni et al. 2013; Magnelli et al. 2011, 2013) and UV (blue data points Steidel et al. 1999; Sawicki & Thompson 2006b; Reddy & Steidel 2009; Alavi et al. 2014) luminosity functions. The conversion of IR luminosities into SFRs was done using the Kennicutt & Evans (2012) calibration. The SFR function from IR data can be directly compared to the SFR function yielded by the model (solid black line) because the star formation in these IR-bright galaxies is almost entirely dust-obscured and the contribution of older stars to dust heating is negligible. The dot-dashed blue lines show the model SFR functions as determined from Equation (4) with $k_{UV} = 1.0 \times 10^{28}\ \text{erg s}^{-1}\ \text{Hz}^{-1}\ M_{\odot}^{-1}\ \text{yr}$, applied to “observed” (i.e., attenuated by dust) UV luminosities, and therefore these curves can be directly compared with the observed UV data, uncorrected for attenuation. The dot-dashed blue lines converge to the black lines at low SFRs, for which the dust attenuation is small.

(A color version of this figure is available in the online journal.)

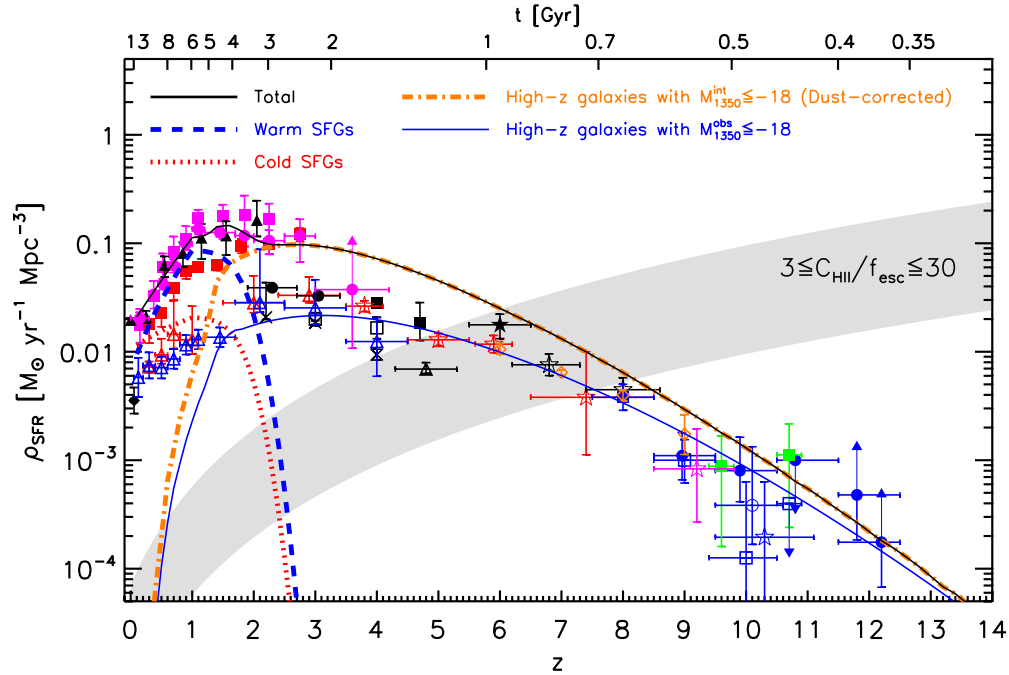


Figure 10. History of cosmic SFR density. The solid black line shows the global value, which is the sum of the contributions of warm (dashed blue line) and cold (dotted red line) late-type galaxies and of proto-spheroidal galaxies with intrinsic $M_{1350}^{\text{int}} \leq -18$ (dot-dashed orange line, that overlaps the solid black line for $z > 2$). The SFR density of late-type galaxies was computed using the Cai et al. (2013) model; that of proto-spheroidal galaxies was computed with the present model, including halo masses $\log(M_{\text{vir}}/M_{\odot}) \geq 8.5$. The solid blue line shows the evolution, as given by our model, of the SFR density of galaxies with observed (i.e., attenuated by dust) magnitudes brighter than $M_{1350}^{\text{obs}} = -18$, already represented in the observed UV luminosity functions. The gray region illustrates the minimum SFR densities required to keep the universe fully ionized if $3 \leq C_{\text{HII}}/f_{\text{esc}} \leq 30$ (Madau et al. 1999; see also Equation (21)). Observational estimates of SFR densities from UV data are from Wyder et al. (2005; filled black diamond), Schiminovich et al. (2005; open red triangles), Cucciati et al. (2012; open blue triangles), Sawicki & Thompson (2006b; black crosses), Steidel et al. (1999; open black squares), Yoshida et al. (2006; filled black squares), Iwata et al. (2007; open black triangle), Reddy & Steidel (2009; open black circles), Bouwens et al. (2006, 2007, 2011a, 2011b, 2013; filled black star, open red stars, open blue star, open black stars, and open magenta stars, respectively), Oesch et al. (2012, 2013a, 2013b; filled blue square, open blue square, open blue circle, open blue circle, respectively), McLure et al. (2013; open orange diamonds), and Ellis et al. (2013; filled blue circles). For completeness we also show SFR densities inferred from far-IR/sub-mm (Rodighiero et al. 2010; Gruppioni et al. 2013; Magnelli et al. 2013; filled magenta squares, filled magenta circles, and filled black triangles, respectively), and radio (Karim et al. 2011; filled red squares) data.

(A color version of this figure is available in the online journal.)

fraction that escapes absorption by dust. It is thus a sensitive probe of the rate at which such photons can escape into the IGM, ionizing it. Equipped with the information obtained from the redshift-dependent Ly α line LFs, and taking into account recent measurements of the ratio of non-ionizing UV to Lyman-continuum emission, in Section 4.2 we evaluate the injection rate of ionizing photons into the IGM and discuss the cosmic reionization. This is done for several choices, taken from the literature, of the IGM clumping factor, which is an ingredient not provided by the model. The results are discussed vis-a-vis a variety of observational constraints including those from the electron scattering optical depth measured by CMB experiments.

4.1. Ly α Emitters

The ionizing photons ($\lambda \leq 912 \text{ \AA}$) can be absorbed by both dust and H I. About 2/3 of those absorbed by H I are converted into Ly α photons (Osterbrock 1989; Santos 2004), so that the LFs of LAEs provide information on their production rate. The Ly α line luminosity before extinction is then

$$L_{\text{Ly}\alpha}^{\text{int}} = \frac{2}{3} \dot{N}_{912}^{\text{int}} f_{912}^{\text{dust}} (1 - f_{912}^{\text{H I}}) h_{\text{P}} \nu_{\text{Ly}\alpha}, \quad (10)$$

where $\dot{N}_{912}^{\text{int}}$ is the production rate of ionizing photons, while $f_{912}^{\text{dust}} = \exp(-\tau_{\text{dust,ion}})$ and $f_{912}^{\text{H I}} = \exp(-\tau_{\text{H I}})$ are the fractions that escape absorption by dust and by H I, respectively, and h_{P} is the Planck constant. We model $\tau_{\text{H I}}$ as

$$\tau_{\text{H I}} = \tau_{\text{H I}}^0 \left(\frac{\dot{M}_{\star}}{M_{\odot} \text{ yr}^{-1}} \right)^{\alpha_{\text{H I}}} + \beta_{\text{H I}}, \quad (11)$$

where the first term on the right-hand side refers to the contribution from high density star-forming regions, while the second term refers to the contribution of diffuse H I. Since the Calzetti et al. (2000) law does not provide the dust absorption optical depth of ionizing photons, we set

$$\tau_{\text{dust,ion}} = A_{912}/1.08 = \gamma A_{1350}/1.08 \quad (12)$$

where A_{1350} is given by Equation (2) and γ is a parameter of the model.

The evolution with the galactic age $\dot{N}_{912}^{\text{int}}$, for a Chabrier (2003) IMF, a constant SFR of $1 M_{\odot} \text{ yr}^{-1}$, and three values of the gas metallicity is illustrated by Figure 11. We adopt an effective ratio $k_{\text{ion}} \equiv \dot{N}_{912}^{\text{int}}/\dot{M}_{\star} = 4.0 \times 10^{53} \text{ photons s}^{-1} M_{\odot}^{-1} \text{ yr}$, appropriate for the typical galactic ages and metallicities of our sources. The figure also shows the evolution of the intrinsic ratio of Lyman-continuum ($\lambda \leq 912 \text{ \AA}$; $L_{912}^{\text{int}} = \dot{N}_{912}^{\text{int}} h_{\text{P}} \text{ erg s}^{-1} \text{ Hz}^{-1}$) to UV luminosity at 1350 \AA , $R_{\text{int}} \equiv L_{912}^{\text{int}}/L_{1350}^{\text{int}}$. For our choice of k_{ion} and k_{UV} (Equation (4)) we have $R_{\text{int}} \simeq 0.265$.

The interstellar dust attenuates $L_{\text{Ly}\alpha}^{\text{int}}$ by a factor $f_{\text{Ly}\alpha}^{\text{dust}} = \exp(-\tau_{\text{Ly}\alpha}^{\text{dust}})$, where $\tau_{\text{Ly}\alpha}^{\text{dust}}$ is the dust optical depth at the Ly α wavelength (1216 \AA). The physical processes governing the escape of Ly α photons from galaxies are complex. Dust content, neutral gas kinematics, and the geometry of the neutral gas seem to play the most important roles. For objects with low dust extinction, such as those relevant here, the detailed calculations of the Ly α radiation transfer by Duval et al. (2014, see their Figures 18 and 19) show that the Ly α is more attenuated than the nearby UV continuum by a factor $\simeq 2$, consistent with the observational result (e.g., Gronwall et al. 2007) that the SFRs

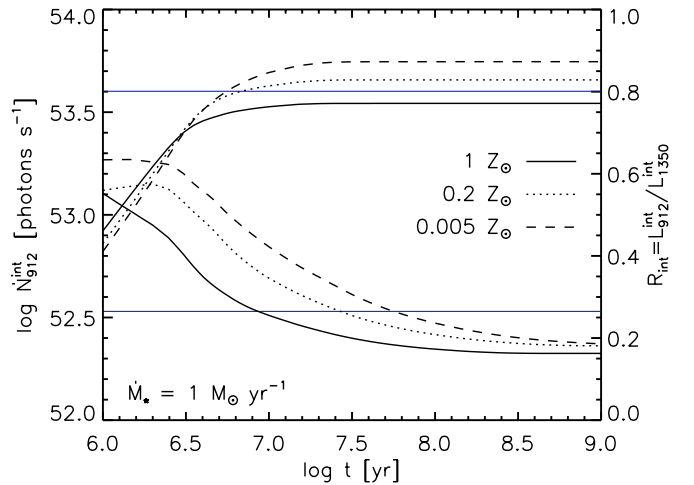


Figure 11. Evolution with galactic age of the production rate of ionizing photons, $\dot{N}_{912}^{\text{int}}$ (left y scale), and of the intrinsic ratio of Lyman-continuum to UV luminosity, $R_{\text{int}} \equiv L_{912}^{\text{int}}/L_{1350}^{\text{int}}$ (right y scale) for a constant SFR, $\dot{M}_{\star} = 1 M_{\odot} \text{ yr}^{-1}$, a Chabrier (2003) IMF, and three metallicities: $Z_{\text{g}} = 0.005$ (dashed line), 0.02 (dotted line), and $1 Z_{\odot}$ (solid line). The chosen reference values, $\dot{N}_{912}^{\text{int}} = 4.0 \times 10^{53}$ and $R_{\text{int}} = 0.265$, are indicated by the upper and lower horizontal lines, respectively.

(A color version of this figure is available in the online journal.)

derived from the Ly α luminosity are $\simeq 3$ times lower than those inferred from the rest-frame UV continuum. With reference to the latter result, it should be noted that part of the attenuation of the Ly α luminosity must be ascribed to the IGM (see below) and that the discrepancy between Ly α and UV continuum SFRs may be due, at least in part, to uncertainties in their estimators. A good fit of the Ly α line LFs is obtained setting $f_{\text{Ly}\alpha}^{\text{dust}} \simeq f_{1216}^{\text{dust}}/1.6$, where $f_{1216}^{\text{dust}} = \exp(-A_{1216}/1.08)$, consistent with the above results.

The fraction $f_{\text{Ly}\alpha}^{\text{IGM}} = \exp(-\tau_{\text{Ly}\alpha}^{\text{IGM}})$ of Ly α photons that survive the passage through the IGM was computed following Madau (1995), taking into account only the absorption of the blue wing of the line

$$f_{\text{Ly}\alpha}^{\text{IGM}} = 0.5 \{1 + \exp[-0.0036(1+z)^{3.46}]\}. \quad (13)$$

The strong attenuation by dust within the galaxy and by H I in the IGM implies that estimates of the SFR of high- z LBGs and LAEs from the observed Ly α luminosity require careful corrections and are correspondingly endowed with large uncertainties. Conversely, the statistics of LAEs and LBGs at high redshifts are sensitive absorption/extinction probes.

Thus the observed Ly α line luminosity writes

$$L_{\text{Ly}\alpha}^{\text{obs}} \simeq 4.36 \times 10^{42} \left(\frac{\dot{M}_{\star}}{M_{\odot} \text{ yr}^{-1}} \right) \times f_{912}^{\text{dust}} (1 - f_{912}^{\text{H I}}) f_{\text{Ly}\alpha}^{\text{dust}} f_{\text{Ly}\alpha}^{\text{IGM}} \text{ erg s}^{-1}. \quad (14)$$

On the whole, this equation contains four parameters: the three parameters in the definition of $\tau_{\text{H I}}$ (Equation (11)), that is, $\tau_{\text{H I}}^0$, $\alpha_{\text{H I}}$, and $\beta_{\text{H I}}$, plus γ (Equation (12)). We have attempted to determine their values fitting the Ly α line LFs by Blanc et al. (2011) at $z \sim 3$ and by Ouchi et al. (2008) at $z \sim 3.8$. However, we could not find an unambiguous solution because of the strong degeneracy among the parameters. To break the parameters' degeneracy, we fixed $\alpha_{\text{H I}} = 0.25$, analogous to Equation (2), and $\tau_{\text{H I}}^0 = 0.3$. Furthermore, we discarded the solutions that imply too high emission rates of ionizing photons and too low

electron scattering optical depth (see below). Based on these somewhat loose criteria, we chose $\beta_{\text{H I}} \simeq 1.5$ and $\gamma \simeq 0.85$.

A check on the validity of our choices is provided by recent Lyman-continuum imaging of galaxies at $z \simeq 3$. Nestor et al. (2013) measured the average ratios of non-ionizing UV to Lyman-continuum flux density corrected for IGM attenuation, η_{obs} , for a sample of LBGs and a sample of LAEs, both at $z \sim 3$. Such ratios were found to be $\eta_{\text{LBG}} = 18.0_{-7.4}^{+34.8}$ for LBGs (rest-frame UV absolute magnitudes $-22 \leq M_{\text{UV}} \leq -20$) and $\eta_{\text{LAE}} = 3.7_{-1.1}^{+2.5}$ for LAEs ($-20 < M_{\text{UV}} \leq -18.3$). Mostardi et al. (2013) probed the Lyman-continuum spectral region of 49 LBGs and 70 LAEs spectroscopically confirmed at $z \sim 2.85$, as well as 58 LAE photometric candidates in the same redshift range. After correcting for foreground galaxy contamination and H I absorption in the IGM, the average values for their samples are $\eta_{\text{LBG}} = 82 \pm 45$, $\eta_{\text{LAE}} = 7.6 \pm 4.1$ for the spectroscopic sample, and $\eta_{\text{LAE}} = 2.6 \pm 0.8$ for the full LAE sample.

The observed ratios are equal to the intrinsic ones $\eta_{\text{int}} \simeq R_{\text{int}}^{-1}$ attenuated by dust and H I absorption (the latter only for ionizing photons)

$$\eta_{\text{obs}} = \eta_{\text{int}} \frac{f_{1350}^{\text{dust}}}{f_{912}^{\text{dust}} \cdot f_{912}^{\text{H I}}}. \quad (15)$$

The intrinsic ratio we have adopted, $\eta_{\text{int}} \simeq R_{\text{int}}^{-1} \simeq 3.77$, is within the range measured for LAEs in both the Nestor et al. (2013) and the Mostardi et al. (2013) samples, implying that the attenuation by dust and H I is small, as expected in the present framework (see Figure 6). LBGs in both samples have SFRs in the range of $5\text{--}250 M_{\odot} \text{ yr}^{-1}$, with median values around $50 M_{\odot} \text{ yr}^{-1}$, and gas metallicities $Z_{\text{g}} \simeq 0.7 \pm 0.3 Z_{\odot}$. After Equation (15) the optical depth for the absorption of ionizing photons by H I is $\tau_{\text{H I, LBG}} = \ln(\eta_{\text{obs, LBG}}/\eta_{\text{int}}) - \ln(f_{1350}^{\text{dust}}/f_{912}^{\text{dust}}) = \ln(\eta_{\text{obs, LBG}}/\eta_{\text{int}}) - (\gamma - 1)A_{1350}/1.08$, giving $\tau_{\text{H I, LBG}} \simeq 1.8_{-0.6}^{+1.3}$ for $\eta_{\text{obs, LBG}} = 18.0_{-7.4}^{+34.8}$ (Nestor et al. 2013) and $\tau_{\text{H I, LBG}} \simeq 3.3_{-0.9}^{+0.6}$ for $\eta_{\text{obs, LBG}} = 82 \pm 45$ (Mostardi et al. 2013). With our choice for the parameters, Equation (11) gives $\tau_{\text{H I}} = \tau_{\text{H I}}^0 \dot{M}_{\star}^{\alpha_{\text{H I}}} + \beta_{\text{H I}} \simeq 2.3_{-0.4}^{+0.4}$, which is consistent with both observational estimates.

As illustrated by Figure 12, the Ly α line LFs yielded by the model compare quite well with observational determinations at several redshifts, from $z = 3$ to $z = 7.7$. The bottom right panel shows that the intrinsic evolution of the Ly α line LF is remarkably weak from $z = 2$ to $z = 6$, it is even weaker than in the UV case (Figure 8), and similarly to the case of the UV LF, its faint portion is predicted to get steeper with increasing redshift. The observed evolution at high- z is more strongly negative than the intrinsic one due to the increasing attenuation by the IGM. The figure also demonstrates that, at $z \geq 5.7$, observational estimates based on photometric samples (open symbols), only partially confirmed in spectroscopy, tend to be systematically higher than those based on purely spectroscopic samples (filled symbols). Therefore, more extensive spectroscopic confirmation is necessary before firm conclusions on the high- z evolution of the Ly α line LF can be drawn.

The average properties, weighted by the halo formation rate, of LAEs at $z = 2, 6$, and 12 are shown as a function of the observed Ly α luminosity in the right-hand panels of Figure 6. Compared to LBGs (left panels of the same figure), LAEs have somewhat younger ages, implying somewhat lower stellar masses, SFRs, and metallicities at given M_{vir} . The latter two factors combine to give a substantially lower dust extinction.

4.2. Escape Fraction of Ionizing Photons and Reionization

The injection rate of ionizing photons into the IGM is

$$\dot{N}_{912}^{\text{esc}} = \dot{N}_{912}^{\text{int}} f_{912}^{\text{esc}} = k_{\text{ion}} \dot{M}_{\star} f_{912}^{\text{esc}} \text{ photons s}^{-1}, \quad (16)$$

where $f_{912}^{\text{esc}} \equiv f_{912}^{\text{dust}} \times f_{912}^{\text{H I}}$ is the fraction of ionizing photons emerging at the galaxy boundary. The dependencies on UV magnitude and redshift of f_{912}^{dust} , $f_{912}^{\text{H I}}$, and f_{912}^{esc} , weighted by the halo formation rate, are illustrated in Figure 13.

As shown by Equations (2) and (11), the optical depths for absorption by both dust and H I (and thus the corresponding escape fractions) are determined by the intrinsic properties of the galaxies (the SFR and, in the case of dust absorption, the metallicity), mostly controlled by the halo mass. They are thus weakly dependent on redshift. Lower-mass galaxies have lower SFRs and, more importantly, lower metallicities. This translates into substantially lower optical depths (< 1) (i.e., substantially higher escape fractions). For brighter galaxies, which have optical depths ≥ 1 , the escape fractions are exponentially sensitive to the weak redshift dependence of the metallicity at a given halo mass (see Figure 2). Thus the small decrease with z of the metallicity translates, for bright galaxies, into a significant increase of f_{912}^{dust} . These luminosity and redshift dependencies do not apply to $f_{912}^{\text{H I}}$, which, not being affected by metallicity, is almost redshift independent at all luminosities. In the bottom right panel of Figure 13 the escape fractions of ionizing photons given by the model for two ranges of observed UV luminosity, are compared with observational estimates at several redshifts. The agreement is generally good.

The redshift-dependent emission rate function, $\phi(\log \dot{N}_{912}^{\text{esc}}, z)$, can be constructed in the same way as the UV LF (Section 3). The average injection rate of ionizing photons into the IGM per unit comoving volume at redshift z is

$$\langle \dot{N}_{912}^{\text{esc}} \rangle(z) = \int \dot{N}_{912}^{\text{esc}} \phi(\log \dot{N}_{912}^{\text{esc}}, z) d \log \dot{N}_{912}^{\text{esc}}. \quad (17)$$

Figure 14 compares the average injection rate of ionizing photons into the IGM, $\langle \dot{N}_{912}^{\text{esc}} \rangle(z)$, as a function of redshift yielded by the model for two choices of the critical halo mass ($M_{\text{crit}} = 10^{8.5} M_{\odot}$ and $M_{\text{crit}} = 10^{10} M_{\odot}$) with observational estimates. The original data refer to different quantities such as the proper hydrogen photoionization rate, $\Gamma_{\text{H I}}(z)$; the average specific intensity of UV background, $J_{\nu}(z)$; and the comoving spatially averaged emissivity, $\epsilon_{\nu}(z)$. The conversion of these quantities into $\langle \dot{N}_{912}^{\text{esc}} \rangle(z)$ was done using the formalism laid down by Kuhlen & Faucher-Giguère (2012). The values of $\langle \dot{N}_{912}^{\text{esc}} \rangle$ obtained from the model are above the estimates by Kuhlen & Faucher-Giguère (2012), but consistent with (although on the high side of) the more recent results by Becker & Bolton (2013) and Nestor et al. (2013).

The reionization of the IGM is described in terms of the evolution of the volume filling factor of H II regions, $Q_{\text{H II}}(t)$, which is ruled by (Madau et al. 1999)

$$\frac{dQ_{\text{H II}}}{dt} \simeq \frac{\langle \dot{N}_{912}^{\text{esc}} \rangle}{\bar{n}_{\text{H}}} - \frac{Q_{\text{H II}}}{\bar{t}_{\text{rec}}}, \quad (18)$$

where $\bar{n}_{\text{H}} = X \rho_{\text{c}} \Omega_{\text{b}} / m_{\text{p}} \simeq 2.5 \times 10^{-7} X (\Omega_{\text{b}} h^2 / 0.022) \text{ cm}^{-3}$ is the mean comoving hydrogen number density in terms of the primordial mass fraction of hydrogen $X = 0.75$, of the present day critical density $\rho_{\text{c}} = 1.878 h^2 \times 10^{-29} \text{ g cm}^{-3}$, and of the proton mass $m_{\text{p}} = 1.67 \times 10^{-24} \text{ g}$. The mean recombination

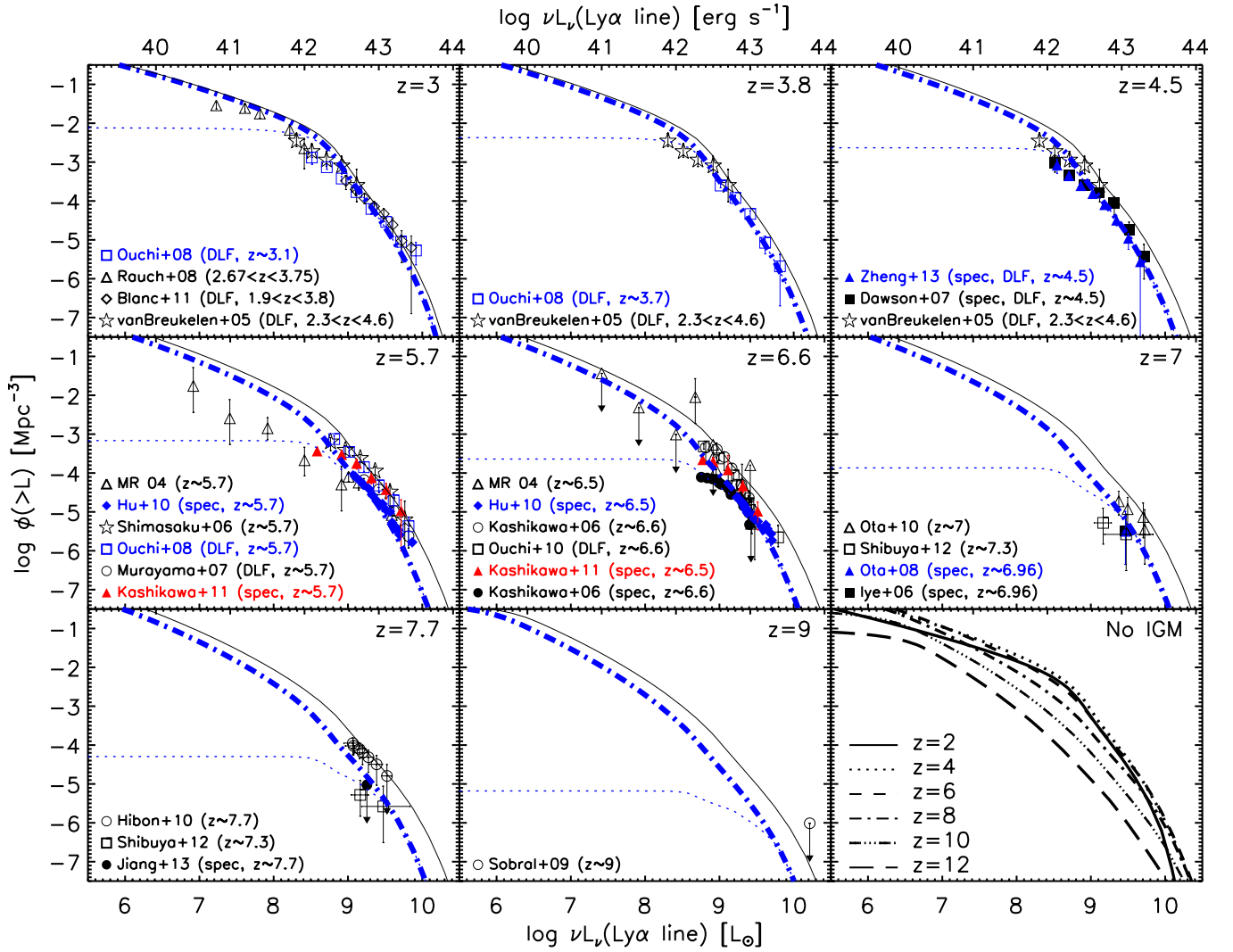


Figure 12. Model cumulative Ly α line luminosity functions at several redshifts, specified in the upper right corner of each panel corrected (solid black lines) and uncorrected (dot-dashed blue lines) for attenuation by the IGM, which are computed following Madau (1995). We have adopted a minimum halo mass of $10^{8.5} M_{\odot}$. The dotted blue lines give the contributions of halo masses $\geq 10^{11} M_{\odot}$. The bottom right panel illustrates the evolution of the Ly α line luminosity function without attenuation by the IGM. The data are from Ouchi et al. (2003), Malhotra & Rhoads (2004, MR 04), van Breukelen et al. (2005), Shimasaku et al. (2006), Iye et al. (2006), Kashikawa et al. (2006, 2011), Dawson et al. (2007), Murayama et al. (2007), Rauch et al. (2008), Ouchi et al. (2008, 2010), Ota et al. (2008, 2010), Sobral et al. (2009), Hibon et al. (2010), Hu et al. (2010), Blanc et al. (2011), Shibuya et al. (2012), Zheng et al. (2013), and Jiang et al. (2013). The data based on spectroscopic samples are shown by filled symbols and the references within the panels are labeled “spec.” Those based on photometric samples are shown by open symbols. The label “DLF” associated to references means that the original papers gave the differential luminosity functions.

(A color version of this figure is available in the online journal.)

time is given by (Madau et al. 1999; Kuhlen & Faucher-Giguère 2012)

$$\begin{aligned} \bar{t}_{\text{rec}} &= \frac{1}{f_e \bar{n}_{\text{H}} (1+z)^3 \alpha_{\text{B}}(T_0) C_{\text{HII}}} \\ &= \frac{0.51}{f_e} \left(\frac{\Omega_{\text{b}}}{0.049} \right)^{-1} \left(\frac{1+z}{7} \right)^{-3} \left(\frac{T_0}{2 \times 10^4 \text{ K}} \right)^{0.7} \\ &\quad \times \left(\frac{C_{\text{HII}}}{6} \right)^{-1} \text{ Gyr}, \end{aligned} \quad (19)$$

where f_e is the number of free electrons per hydrogen nucleus in the ionized IGM, assumed to have a temperature $T_0 = 2 \times 10^4$ K, and $C_{\text{HII}} \equiv \langle \rho_{\text{HII}}^2 \rangle / \langle \rho_{\text{HII}} \rangle^2$ is the clumping factor of the ionized hydrogen. f_e depends on the ionization state of helium; we assumed it to be doubly ionized ($f_e = 1 + Y/2X \simeq 1.167$) at $z < 4$ and singly ionized ($f_e = 1 + Y/4X \simeq 1.083$) at higher redshifts (Robertson et al. 2013).

The clumping factor has been extensively investigated using numerical simulations (see Finlator et al. 2012 for a critical discussion of earlier work). A series of drawbacks have been progressively discovered and corrected. The latest studies accounting for the photo-ionization heating that tends to smooth the diffuse IGM, and for the IGM temperature, which could suppress the recombination rate further, generally find relatively low values of C_{HII} (Pawlik et al. 2009; McQuinn et al. 2011; Shull et al. 2012; Finlator et al. 2012; Kuhlen & Faucher-Giguère 2012; see the upper left panel of Figure 15). Alternatively, the clumping factor can be computed as the second moment of the IGM density distribution, integrating up to a maximum overdensity (Kulkarni et al. 2013). We adopt, as our reference, the model $C_{\text{HII}, T_{\text{b}}, x_{\text{HII}} > 0.95}$ by Finlator et al. (2012), but we will also discuss the effect of different choices.

Additional constraints on the reionization history are set by the electron scattering optical depth, τ_{es} , measured by CMB anisotropy experiments. The optical depth of electron scattering

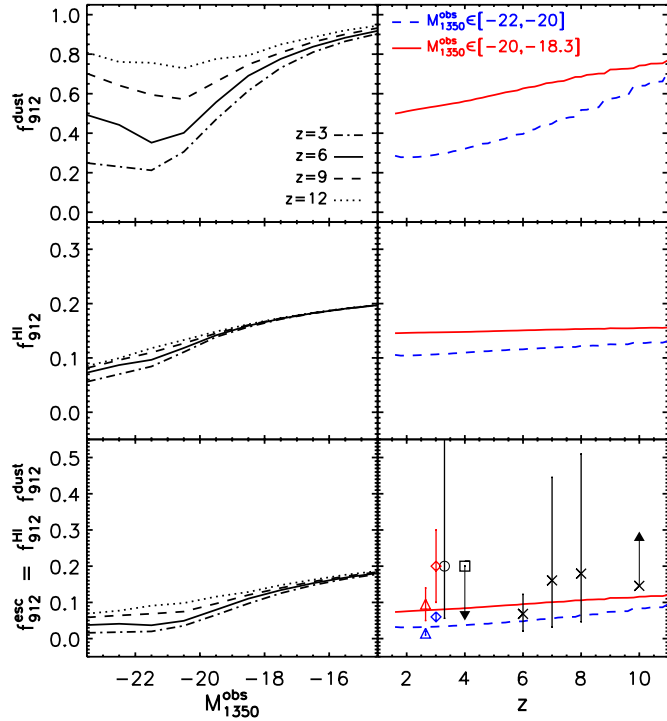


Figure 13. Left panels: fractions of ionizing photons surviving dust, H I, and both absorptions (f_{912}^{dust} , f_{912}^{HI} , and f_{912}^{esc} , from top to bottom), weighted by the halo formation rate and yielded by our model for $z_{\text{obs}} = 3$ (dot-dashed line), 6 (solid line), 9 (dashed line), and 12 (dotted line) as a function of the attenuated UV luminosity M_{1350}^{obs} . Right panels: escape fractions given by the model as a function of z for two luminosity bins, that is, $M_{1350}^{\text{obs}} \in [-22, -20]$ (dashed blue line) and $M_{1350}^{\text{obs}} \in [-20, -18.3]$ (solid red line). Data in the bottom right panel are from: Iwata et al. (2009) at $z \simeq 3.1$ (offset by $\Delta z = 0.2$ for readability, the open circle corresponds to the median value and the error bars extend to the minimum/maximum values); Nestor et al. (2013) for LBGs ($M_{\text{UV}} \in [-22, -20]$, open blue diamond) and for LAEs ($M_{\text{UV}} \in [-20, -18.3]$, open red diamond) at $z \sim 3$; Mostardi et al. (2013; open blue triangle and open red triangle for LBGs and LAEs, respectively) at $z \sim 2.85$ (the points are offset by $\Delta z = -0.2$ for readability); Vanzella et al. (2010; open square representing an upper limit at $z \simeq 4$); Mitra et al. (2013; black crosses) for LBGs in the redshift range $6 \leq z \leq 10$.

(A color version of this figure is available in the online journal.)

up to redshift z is given by

$$\begin{aligned} \tau_{\text{es}}(\leq z) &= \int_0^z dz' \left| \frac{dt}{dz'} \right| c \sigma_{\text{T}} n_e(z') \\ &= \int_0^z dz' \frac{c(1+z')^2}{H_0 \sqrt{\Omega_{\Lambda} + \Omega_{\text{m}}(1+z')^3}} f_e Q_{\text{HII}}(z') \sigma_{\text{T}} \bar{n}_{\text{H}}, \end{aligned} \quad (20)$$

where $n_e \simeq f_e Q_{\text{HII}} \bar{n}_{\text{H}} (1+z)^3$ is the mean electron density, c is the speed of light, and $\sigma_{\text{T}} \simeq 6.65 \times 10^{-25} \text{ cm}^2$ is the Thomson cross section. *WMAP* 9 yr data alone give $\tau_{\text{es}} = 0.089 \pm 0.014$, which slightly decrease to $\tau_{\text{es}} = 0.081 \pm 0.012$ when they are combined with external data sets (Hinshaw et al. 2013). The combination of the *Planck* temperature power spectrum with a *WMAP* polarization, low-multipole likelihood results in an estimate closely matching the *WMAP* 9 yr value, $\tau_{\text{es}} = 0.089^{+0.012}_{-0.014}$ (Planck Collaboration 2013b). However, replacing the *WMAP* polarized dust template with the far more sensitive *Planck*/HFI 353 GHz polarization map lowers the best fit value to $\tau_{\text{es}} = 0.075 \pm 0.013$ (Planck Collaboration 2013a); this result, however, has to be taken as preliminary.

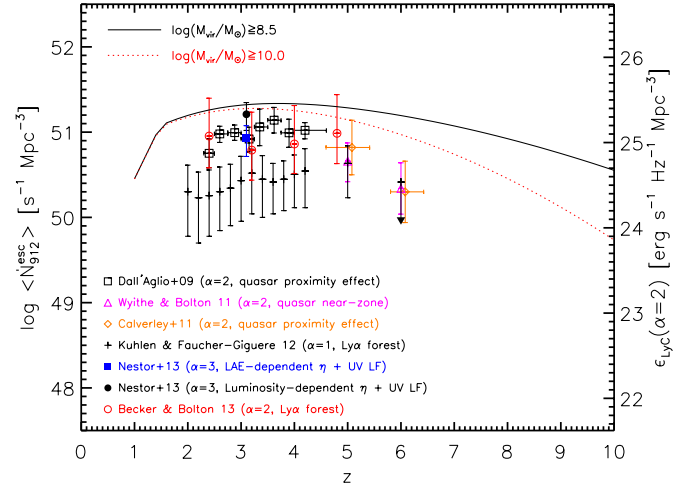


Figure 14. Comoving emission rates of ionizing photons ($\langle \dot{N}_{912}^{\text{esc}} \rangle$, left y scale) and ionizing emissivities ($\epsilon_{\text{LYC}} \simeq \langle \dot{N}_{912}^{\text{esc}} \rangle h \rho \alpha$ for $\epsilon(\nu) = \epsilon_{\text{LYC}}(\nu/\nu_{912})^{-\alpha}$ with $\alpha = 2$, right y scale) as a function of redshift. The solid black line and the dotted red line correspond to critical halo masses of $10^{8.5}$ and $10^{10} M_{\odot}$, respectively. Data points are from Dall'Aglio et al. (2009), Wyithe & Bolton (2011), Calverley et al. (2011), Kuhlen & Faucher-Giguère (2012), Becker & Bolton (2013), and Nestor et al. (2013).

(A color version of this figure is available in the online journal.)

The evolution of $Q_{\text{HII}}(t)$ and the electron scattering optical depth $\tau_{\text{es}}(\leq z)$ yielded by the model adopting the critical halo mass $M_{\text{crit}} = 10^{8.5} M_{\odot}$, the effective escape fraction f_{912}^{esc} laid down before, and the evolutionary law for the IGM clumping factor C_{HII} by Finlator et al. (2012), are shown by the thick, solid black lines in the main panel of Figure 15. Although this model gives a τ_{es} consistent with the determination by Planck Collaboration (2013b) and less than 2σ below those by Hinshaw et al. (2013) and Planck Collaboration (2013b), it yields a more extended fully ionized phase than indicated by the constraints on Q_{HII} at $z \geq 6$, which were collected by Robertson et al. (2013) who, however, cautioned that they are all subject to substantial systematic or modeling uncertainties. Indications pointing to a rapid drop of the ionization degree above $z \simeq 6$ include hints of a decrease of the comoving emission rates of ionizing photons (see Figure 14), sizes of quasar near zones, and the Ly α transmission through the IGM (see Robertson et al. 2013 for references).

As we have seen before, the observed UV LFs imply $M_{\text{crit}} \lesssim 10^{10} M_{\odot}$. Adopting the latter value and keeping our baseline $f_{912}^{\text{esc}}(z)$ and $C_{\text{HII}}(z)$ shortens the fully ionized phase that now extends only up to $z \sim 6$ (dotted red line in the main figure of Figure 15), lessening the discrepancy with constraints on Q_{HII} at the cost of τ_{es} , dropping almost $\simeq 3\sigma$ below the best fit *WMAP* value and 2σ below the best fit value of Planck Collaboration (2013a). This conclusion is unaffected by different choices for $C_{\text{HII}}(z)$, as illustrated in the upper left panel of Figure 15, as long as we keep our baseline $f_{912}^{\text{esc}}(z)$. This is because the production rate of ionizing photons (first term on the right-hand side of Equation (18)) is always substantially larger than the recombination rate.

The minimum SFR density required to keep the universe fully ionized at the redshift z is (Madau et al. 1999)

$$\dot{\rho}_{\star} \simeq 8.2 \times 10^{-4} \left(\frac{C_{\text{HII}}}{f_{\text{esc}}} \right) \left(\frac{\Omega_{\text{b}} h^2}{0.022} \right)^2 \left(\frac{1+z}{7} \right)^3 M_{\odot} \text{ yr}^{-1} \text{ Mpc}^{-3}. \quad (21)$$

This is shown in Figure 10 (gray area) for $3 \lesssim C_{\text{HII}}/f_{\text{esc}} \lesssim 30$. A similar figure was presented by Finkelstein et al. (2012, their

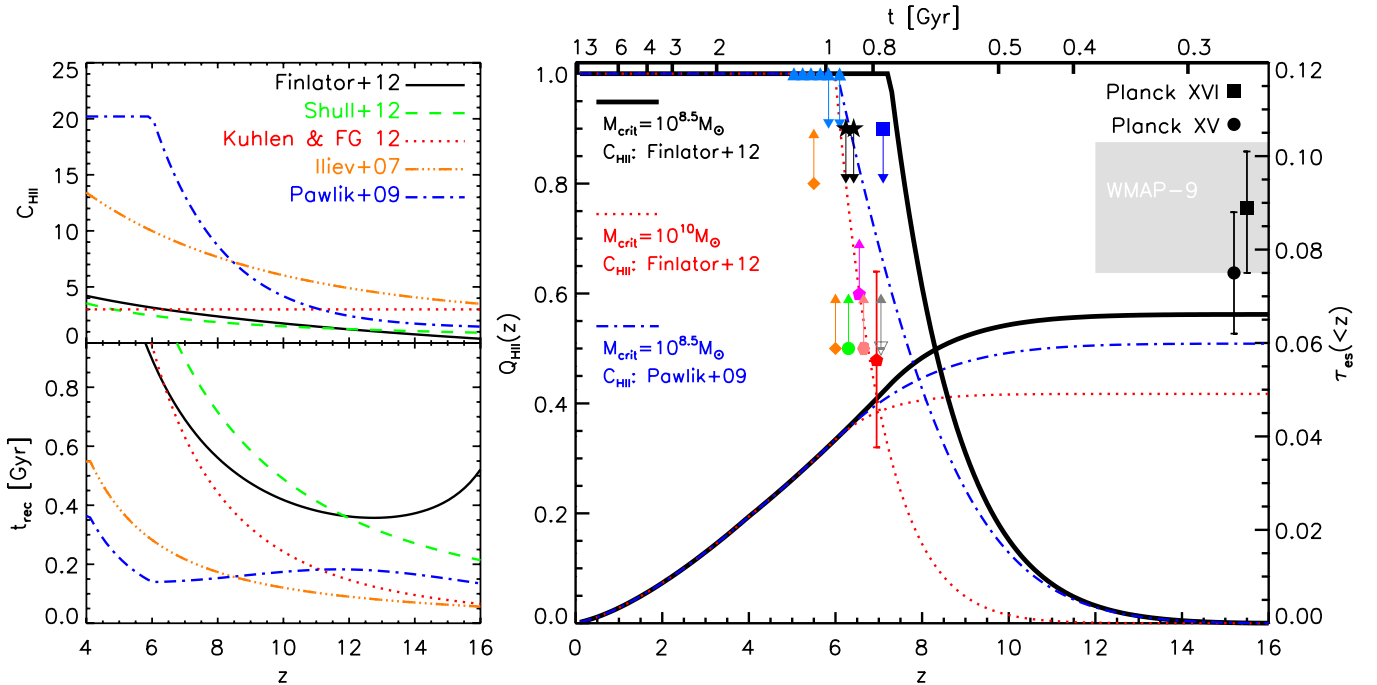


Figure 15. Left panels: evolutionary laws for the IGM clumping factor C_{HII} (upper panel) proposed in the literature and the corresponding recombination timescales t_{rec} (lower panel). Solid black line: $C_{\text{HII}}(z) = 9.25 - 7.21 \log(1+z)$ (Finlator et al. 2012); dashed green line: $C_{\text{HII}}(z) = 2.9[(1+z)/6]^{-1.1}$ (Shull et al. 2012); dotted red line: $C_{\text{HII}}(z) = 3$ (Kuhlen & Faucher-Giguère 2012); triple-dot-dashed orange line: $C_{\text{HII}}(z) = 26.2917 \exp(-0.1822z + 0.003505z^2)$ (Iliev et al. 2007); dot-dashed blue line: $C_{\text{HII}}(z) = \min[C_{\text{HII}}(z=6), \exp(-0.47z + 5.76) + 1.29]$, corresponding to the C_{-1} L6N256 no-reheating simulation by Pawlik et al. (2009) covering the range $6 \leq z \leq 20$. Main figure: evolution with the redshift of the volume filling factor Q_{HII} (left y scale) and of the electron optical depth τ_{es} (right y scale). The thick solid black lines correspond to the fiducial model with $C_{\text{HII}}(z)$ by Finlator et al. (2012) and $M_{\text{crit}} = 10^{8.5} M_{\odot}$. The dotted red lines correspond to the same model, but with $M_{\text{crit}} = 10^{10} M_{\odot}$. The dot-dashed blue lines show the results with the $C_{\text{HII}}(z)$ by Pawlik et al. (2009) for $M_{\text{crit}} = 10^{8.5} M_{\odot}$. The observational constraints on the volume filling factor are from a collection of literature data made by Robertson et al. (2013). The 9 yr WMAP constraint on electron optical depth, $\tau_{\text{es}} = 0.089 \pm 0.014$ (Hinshaw et al. 2013), is represented by the gray region while the filled square and the filled circle with error bars represent the preliminary estimates by Planck Collaboration (2013b) and Planck Collaboration (2013a), respectively.

(A color version of this figure is available in the online journal.)

Figure 3). A comparison of their green curve with our blue curve illustrates the difference between the UV luminosity density implied by our model for sources brighter than $M_{\text{UV}} = -18$ and that from the hydrodynamic simulations of Finlator et al. (2011a).

A sort of tradeoff between the constraints of Q_{HII} and those of τ_{es} is obtained if the cooling rate of HII increases rapidly with decreasing z for $z \lesssim 8$. This might be the case if, for example, the clumping factor climbs in this redshift range, as in the C_{-1} L6N256 no-reheating simulation by Pawlik et al. (2009; dot-dashed blue line in the main figure of Figure 15). The drawbacks suffered by these simulations were, however, pointed out by Pawlik et al. (2009) and Finlator et al. (2012).

The tension between the determinations of $\tau_{\text{es}}(\leq z)$ and constraints on $Q_{\text{HII}}(z)$ has been repeatedly discussed in recent years (e.g., Kuhlen & Faucher-Giguère 2012; Haardt & Madau 2012; Robertson et al. 2013). Our conclusions are broadly consistent with the earlier ones, as can be seen by all models matching the observed high- z UV LFs. However, our model differs from the others because our LFs and the escape fraction as a function of redshift are physically grounded, whereas the quoted models are based on phenomenological fits to the data. This means that our model is more constrained; for example, the extrapolations of the LFs outside the luminosity and redshift ranges covered by observations come out from our equations, rather than being controlled by adjustable parameters. In other words we explore different parameter spaces. As a result, we differ in important details such as the slope of the faint tail of the UV LF and its redshift dependence, the total number density of

high- z UV galaxies, and the redshift dependence of the escape fraction of ionizing photons.

The need for a redshift- or mass dependence of f_{912}^{esc} has also been deduced by other studies (e.g., Alvarez et al. 2012; Mitra et al. 2013). Mitra et al. (2013) combined data-constrained reionization histories and the evolution of the LF of early galaxies to find an empirical indication of a 2.6 times increase of the average escape fraction from $z = 6$ to $z = 8$. Alvarez et al. (2012) argued that there are both theoretical and observational indications that f_{912}^{esc} is higher at lower halo masses and proposed that a faint population of galaxies with host halo masses of $\sim 10^{8-9} M_{\odot}$ dominated the ionizing photon budget at redshifts $z \gtrsim 9$ due to their much higher escape fractions, which were again empirically estimated. Our model provides a physical basis for the increase of the effective f_{912}^{esc} with mass and redshift.

The present data do not allow us to draw any firm conclusion on the reionization history because they may be affected by substantial uncertainties. Those uncertainties on data at $z = 6-7$ are discussed by Robertson et al. (2013). Those on τ_{es} are illustrated by the finding (Planck Collaboration 2013a) that different corrections for the contamination by polarized foregrounds may lower the best fit value by about 1σ .

5. CONCLUSIONS

We have worked out a physical model for the evolution of the UV LF of high- z galaxies and for the reionization history. The LF is directly linked to the formation rate of virialized halos and to the cooling and heating processes governing the

star formation. For the low halo masses and young galactic ages of interest here it is not enough to take into account SN and AGN feedback, as is usually done for halo masses $M_{\text{vir}} \gtrsim 10^{11} M_{\odot}$, because other heating processes—such as the radiation from massive low-metallicity stars, stellar winds, and the UV background—can contribute to reducing and eventually quenching the SFR. We have modeled this by increasing the efficiency of cold gas removal and introducing a lower limit, M_{crit} , to halo masses that can host active star formation.

Another still open issue is the production rate of UV photons per unit halo mass at high z , which is influenced by two competing effects. On one side, the expected increase with redshift of the Jeans mass, hence of the characteristic stellar mass, entails a higher efficiency in the production of UV photons. On the other hand, more UV photons imply more gas heating (i.e., a decrease of the SFR). We find that the observed UV LFs up to the highest redshifts are very well reproduced with the SFRs yielded by the model and the extinction law of Equation (2) for a production rate of UV photons corresponding to a Chabrier (2003) IMF.

The observed UV LFs (Figure 8) constrain M_{crit} to be $\lesssim 10^{10} M_{\odot}$, which is consistent with estimates from simulations. Figure 8 highlights several features of the model: (1) dust extinction is higher for higher luminosities, associated to more massive halos that have a faster metal enrichment; (2) the higher feedback efficiency in less massive halos makes the slope of the faint end of the LF flatter than that of the halo formation rate, yet the former reflects to some extent the steepening with increasing z of the latter, which has important implications for the sources of the ionizing background at high z ; and (3) the evolution of the LF from $z = 2$ to $z = 6$ is weak because the decrease with increasing redshift of the halo formation rate in the relevant range of halo masses is largely compensated by the increase of the star formation efficiency due to the faster gas cooling and by the increase of dust extinction with increasing halo mass.

Another key property of the model (Figure 2) is the fast metal enrichment of the more massive galaxies that translates into a rapid increase of dust obscuration. Therefore, these galaxies show up mostly at far-IR/(sub-)millimeter wavelengths, a prediction successfully tested against observational data (Figures 9 and 10). The model thus predicts a strong correlation between dust attenuation and halo/stellar mass for UV selected high- z galaxies. The ratio of dust-obscured to unobscured star formation has a broad maximum at $z \simeq 2$ –3. The decrease at lower redshifts is due to the decreasing amount of ISM in galaxies; at higher redshifts it is related to the fast decrease of the abundance of massive halos where the metal enrichment and, correspondingly, the dust extinction grow fast.

Similarly, good fits are obtained for the Ly α line LFs (Figure 12) that provide information on the production rate of ionizing photons and on their absorption by neutral interstellar hydrogen. Further constraints on the attenuation by dust and H I are provided by recent measurements (Nestor et al. 2013; Mostardi et al. 2013) of the observed ratios of non-ionizing UV to Lyman-continuum flux densities for LAEs and LBGs. These data have allowed us to derive a simple relationship between the optical depth for H I absorption and SFR. Taking this relation into account, the model reproduces the very weak evolution of the Ly α line LF between $z = 2$ and $z = 6$, which is even weaker than in the UV.

The derived relationships linking the optical depths for absorption of ionizing photons by dust and H I to the SFR and, in the case of dust absorption, to the metallicity of the galaxies,

imply higher effective escape fractions for galaxies with lower intrinsic UV luminosities or lower halo/stellar masses, as well as a mild increase of the escape fraction with increasing redshift at fixed luminosity or halo/stellar mass. Redshift- or mass-dependencies of the escape fraction were previously empirically deduced by, e.g., Alvarez et al. (2012) and Mitra et al. (2013). Our model provides a physical basis for these dependencies.

At this point we can compute the average injection rate of ionizing photons into the IGM as a function of halo mass and redshift. To reconstruct the ionization history of the universe we need the evolution of the clumping factor of the IGM, for which we have adopted the model $C_{\text{HII}, T_b, x_{\text{HII}} > 0.95}$ by Finlator et al. (2012) as our reference, but also considered alternative models discussed in the literature. With our equation for the escape fraction of ionizing photons we find that galaxies already represented in the observed UV LFs (i.e., with $M_{\text{UV}} \lesssim -18$, hosted by halo masses $\gtrsim 10^{10} M_{\odot}$), can account for a complete ionization of the IGM up to $z \simeq 6$. To get complete ionization up to $z \simeq 7$ the population of star-forming galaxies at this redshift must extend in the luminosity to $M_{\text{UV}} \sim -13$ or fainter, which is in agreement with the conclusions of other analyses (e.g., Robertson et al. 2013). The surface densities of $M_{\text{UV}} \sim -13$ galaxies would correspond to those of halo masses of $\sim 10^{8.5} M_{\odot}$, which are not far from the lower limit on M_{crit} from hydrodynamical simulations.

A complete IGM ionization up to $z \simeq 7$ is not favored by some (admittedly uncertain) data at $z \simeq 6$ –7 collected by Robertson et al. (2013), which point to a fast decline of the ionization degree at $z \gtrsim 6$. However, an even more extended ionized phase is implied by the determinations of electron scattering optical depths, τ_{es} , from CMB experiments. Our model adopting the critical halo mass $M_{\text{crit}} = 10^{8.5} M_{\odot}$, yielding complete ionization up to $z \simeq 7$, gives a τ_{es} consistent with the determination by Planck Collaboration (2013b) and less than 2σ below those by Hinshaw et al. (2013) and Planck Collaboration (2013b). Raising M_{crit} to $10^{10} M_{\odot}$ limits the fully ionized phase to $z \lesssim 6$ and decreases τ_{es} to a value almost $\simeq 3\sigma$ below the estimates by Hinshaw et al. (2013) and Planck Collaboration (2013b) and 2σ below that by Planck Collaboration (2013a). Because all these constraints on the reionization history are affected by substantial uncertainties, any firm conclusion is premature. Better data are needed to resolve the issue.

We are grateful to the referee for a careful reading of the manuscript and many constructive comments that helped us substantially improve the paper. We also acknowledge useful comments from G. Zamorani. Z.Y.C. acknowledges support from the joint PhD project between XMU and SISSA. The work has been supported in part by ASI/INAF agreement No. I/072/09/0 and by PRIN 2009 “Millimeter and sub-millimeter spectroscopy for high resolution studies of primeval galaxies and clusters of galaxies.”

REFERENCES

- Adelberger, K. L., & Steidel, C. C. 2000, *ApJ*, 544, 218
 Alavi, A., Siana, B., Richard, J., et al. 2014, *ApJ*, 780, 143
 Alvarez, M. A., Finlator, K., & Trenti, M. 2012, *ApJL*, 759, L38
 Asplund, M., Grevesse, N., Sauval, A. J., & Scott, P. 2009, *ARA&A*, 47, 481
 Becker, G. D., & Bolton, J. S. 2013, *MNRAS*, 436, 1023
 Blanc, G. A., Adams, J. J., Gebhardt, K., et al. 2011, *ApJ*, 736, 31
 Bouché, N., Murphy, M. T., Kacprzak, G. G., et al. 2013, *Sci*, 341, 50
 Bouwens, R. J., Bradley, L., Zitrin, A., et al. 2013, arXiv:1211.2230
 Bouwens, R. J., Illingworth, G. D., Blakeslee, J. P., & Franx, M. 2006, *ApJ*, 653, 53

- Bouwens, R. J., Illingworth, G. D., Franx, M., & Ford, H. 2007, *ApJ*, 670, 928
- Bouwens, R. J., Illingworth, G. D., Franx, M., & Ford, H. 2008, *ApJ*, 686, 230
- Bouwens, R. J., Illingworth, G. D., Franx, M., et al. 2009, *ApJ*, 705, 936
- Bouwens, R. J., Illingworth, G. D., Labbe, I., et al. 2011a, *Natur*, 469, 504
- Bouwens, R. J., Illingworth, G. D., Oesch, P. A., et al. 2011b, *ApJ*, 737, 90
- Bouwens, R. J., Illingworth, G. D., Oesch, P. A., et al. 2012, *ApJ*, 754, 83
- Bradley, L. D., Trenti, M., Oesch, P. A., et al. 2012, *ApJ*, 760, 108
- Cai, Z.-Y., Lapi, A., Xia, J.-Q., et al. 2013, *ApJ*, 768, 21
- Calverley, A. P., Becker, G. D., Haehnelt, M. G., & Bolton, J. S. 2011, *MNRAS*, 412, 2543
- Calzetti, D., Armus, L., Bohlin, R. C., et al. 2000, *ApJ*, 533, 682
- Caputi, K. I., Lagache, G., Yan, L., et al. 2007, *ApJ*, 660, 97
- Castellano, M., Fontana, A., Grazian, A., et al. 2012, *A&A*, 540, A39
- Chabrier, G. 2003, *PASP*, 115, 763
- Coe, D., Zitrin, A., Carrasco, M., et al. 2013, *ApJ*, 762, 32
- Cucciati, O., Tresse, L., Ilbert, O., et al. 2012, *A&A*, 539, A31
- Cullen, F., Cirasuolo, M., McLure, R. J., & Dunlop, J. S. 2013, arXiv:1310.0816
- Dall'Aglio, A., Wisotzki, L., & Worsack, G. 2009, arXiv:0906.1484
- Davé, R., Finlator, K., Oppenheimer, B. D., et al. 2010, *MNRAS*, 404, 1355
- Dawson, S., Rhoads, J. E., Malhotra, S., et al. 2007, *ApJ*, 671, 1227
- Dayal, P., Dunlop, J. S., Maio, U., & Ciardi, B. 2013, *MNRAS*, 434, 1486
- Dayal, P., Ferrara, A., & Gallerani, S. 2008, *MNRAS*, 389, 1683
- Dayal, P., Ferrara, A., Saro, A., et al. 2009, *MNRAS*, 400, 2000
- Dekel, A., & Birnboim, Y. 2006, *MNRAS*, 368, 2
- Dekel, A., Birnboim, Y., Engel, G., et al. 2009, *Natur*, 457, 451
- Dijkstra, M., Haiman, Z., & Loeb, A. 2004, *ApJ*, 613, 646
- Duval, F., Schaerer, D., Östlin, G., & Laursen, P. 2014, *A&A*, 562, 52
- Ellis, R. S., McLure, R. J., Dunlop, J. S., et al. 2013, *ApJL*, 763, L7
- Erb, D. K., Shapley, A. E., Pettini, M., et al. 2006, *ApJ*, 644, 813
- Fan, L., Lapi, A., Bressan, A., et al. 2010, *ApJ*, 718, 1460
- Fagotto, F., Bressan, A., Bertelli, G., & Chiosi, C. 1994a, *A&AS*, 104, 365
- Fagotto, F., Bressan, A., Bertelli, G., & Chiosi, C. 1994b, *A&AS*, 105, 29
- Fardal, M. A., Katz, N., Weinberg, D. H., & Davé, R. 2007, *MNRAS*, 379, 985
- Finkelstein, S. L., Papovich, C., Ryan, R. E., et al. 2012, *ApJ*, 758, 93
- Finlator, K., Davé, R., & Özel, F. 2011a, *ApJ*, 743, 169
- Finlator, K., Oh, S. P., Özel, F., & Davé, R. 2012, *MNRAS*, 427, 2464
- Finlator, K., Oppenheimer, B. D., & Davé, R. 2011b, *MNRAS*, 410, 1703
- Garel, T., Blaizot, J., Guiderdoni, B., et al. 2012, *MNRAS*, 422, 310
- Gonzalez-Perez, V., Lacey, C. G., Baugh, C. M., et al. 2013, *MNRAS*, 429, 1609
- Granato, G. L., De Zotti, G., Silva, L., Bressan, A., & Danese, L. 2004, *ApJ*, 600, 580
- Gronwall, C., Ciardullo, R., Hickey, T., et al. 2007, *ApJ*, 667, 79
- Grupponi, C., Pozzi, F., Rodighiero, G., et al. 2013, *MNRAS*, 432, 23
- Haardt, F., & Madau, P. 2012, *ApJ*, 746, 125
- Hambrick, D. C., Ostriker, J. P., Johansson, P. H., & Naab, T. 2011, *MNRAS*, 413, 2421
- Hathi, N. P., Malhotra, S., & Rhoads, J. E. 2008, *ApJ*, 673, 686
- Hayes, M., Schaerer, D., Östlin, G., et al. 2011, *ApJ*, 730, 8
- Heinis, S., Buat, V., Bethermin, M., et al. 2014, *MNRAS*, 437, 1268
- Hibon, P., Cuby, J.-G., Willis, J., et al. 2010, *A&A*, 515, 97
- Hinshaw, G., Larson, D., Komatsu, E., et al. 2013, *ApJS*, 208, 19
- Hu, E. M., Cowie, L. L., Barger, A. J., et al. 2010, *ApJ*, 725, 394
- Iliev, I. T., Mellema, G., Shapley, R. J., & Pen, U.-L. 2007, *MNRAS*, 376, 534
- Iwata, I., Inoue, A. K., Matsuda, Y., et al. 2009, *ApJ*, 692, 1287
- Iwata, I., Ohta, K., Tamura, N., et al. 2007, *MNRAS*, 376, 1557
- Iye, M., Ota, K., Kashikawa, N., et al. 2006, *Natur*, 443, 186
- Jaacks, J., Choi, J.-H., Nagamine, K., Thompson, R., & Varghese, S. 2012a, *MNRAS*, 420, 1606
- Jaacks, J., Nagamine, K., & Choi, J. H. 2012b, *MNRAS*, 427, 403
- Jiang, L., Bian, F., Fan, X., et al. 2013, *ApJL*, 771, L6
- Karim, A., Schinnerer, E., Martínez-Sansigre, A., et al. 2011, *ApJ*, 730, 61
- Kashikawa, N., Shimasaku, K., Malkan, M. A., et al. 2006, *ApJ*, 648, 7
- Kashikawa, N., Shimasaku, K., Matsuda, Y., et al. 2011, *ApJ*, 734, 119
- Kennicutt, R. C., & Evans, N. J. 2012, *ARA&A*, 50, 531
- Kereš, D., Katz, N., Weinberg, D. H., & Davé, R. 2005, *MNRAS*, 363, 2
- Kobayashi, M. A. R., Totani, T., & Nagashima, M. 2010, *ApJ*, 708, 1119
- Kravtsov, A. V., Gnedin, O. Y., & Klypin, A. A. 2004, *ApJ*, 609, 482
- Krumholz, M. R., & Dekel, A. 2012, *ApJ*, 753, 16
- Kuhlen, M., & Faucher-Giguère, C.-A. 2012, *MNRAS*, 423, 862
- Kulkarni, G., Rollinde, E., Hennawi, J. F., & Vangioni, E. 2013, *ApJ*, 772, 93
- Lacey, C. G., Baugh, C. M., Frenk, C. S., & Benson, A. J. 2011, *MNRAS*, 412, 1828
- Lapi, A., & Cavaliere, A. 2011, *ApJ*, 743, 127
- Lapi, A., González-Nuevo, J., Fan, L., et al. 2011, *ApJ*, 742, 24
- Lapi, A., Salucci, P., & Danese, L. 2013, *ApJ*, 772, 85
- Lapi, A., Shankar, F., Mao, J., et al. 2006, *ApJ*, 650, 42
- Liu, X., Shapley, A. E., Coil, A. L., Brinchmann, J., & Ma, C.-P. 2008, *ApJ*, 678, 758
- Lo Faro, B., Monaco, P., Vanzella, E., et al. 2009, *MNRAS*, 399, 827
- Lorenzoni, S., Bunker, A. J., Wilkins, S. M., et al. 2011, *MNRAS*, 414, 1455
- Lorenzoni, S., Bunker, A. J., Wilkins, S. M., et al. 2013, *MNRAS*, 429, 150
- Madau, P. 1995, *ApJ*, 441, 18
- Madau, P., Haardt, F., & Rees, M. J. 1999, *ApJ*, 514, 648
- Magnelli, B., Elbaz, D., Chary, R. R., et al. 2011, *A&A*, 528, A35
- Magnelli, B., Popesso, P., Berta, S., et al. 2013, *A&A*, 553, A132
- Maiolino, R., Nagao, T., Grazian, A., et al. 2008, *A&A*, 488, 463
- Malhotra, S., & Rhoads, J. E. 2004, *ApJ*, 617, 5
- Mannucci, F., Cresci, G., Maiolino, R., Marconi, A., & Gnerucci, A. 2010, *MNRAS*, 408, 2115
- Mao, J., Lapi, A., Granato, G. L., de Zotti, G., & Danese, L. 2007, *ApJ*, 667, 655
- McLure, R. J., Dunlop, J. S., Bowler, R. A. A., et al. 2013, *MNRAS*, 432, 2696
- McLure, R. J., Dunlop, J. S., Cirasuolo, M., et al. 2010, *MNRAS*, 403, 960
- McQuinn, M., Oh, S. P., & Faucher-Giguère, C.-A. 2011, *ApJ*, 743, 82
- Mitra, S., Ferrara, A., & Choudhury, T. R. 2013, *MNRAS*, 428, L1
- Mostardi, R. E., Shapley, A. E., Nestor, D. B., et al. 2013, *ApJ*, 779, 65
- Muñoz, J. A. 2012, *JCAP*, 4, 15
- Muñoz, J. A., & Loeb, A. 2011, *ApJ*, 729, 99
- Murayama, T., Taniguchi, Y., Scoville, N. Z., et al. 2007, *ApJS*, 172, 523
- Nagamine, K., Ouchi, M., Springel, V., & Hernquist, L. 2010, *PASJ*, 62, 1455
- Navarro, J. F., Frenk, C. S., & White, S. D. M. 1997, *ApJ*, 490, 493
- Nestor, D. B., Shapley, A. E., Kornei, K. A., Steidel, C. C., & Siana, B. 2013, *ApJ*, 765, 47
- Oesch, P. A., Bouwens, R. J., Illingworth, G. D., et al. 2012, *ApJ*, 759, 135
- Oesch, P. A., Bouwens, R. J., Illingworth, G. D., et al. 2013a, *ApJ*, 773, 75
- Oesch, P. A., Bouwens, R. J., Illingworth, G. D., et al. 2013b, arXiv:1309.2280
- Oesch, P. A., Labbé, I., Bouwens, R. J., et al. 2013c, *ApJ*, 772, 136
- Okamoto, T., Gao, L., & Theuns, T. 2008, *MNRAS*, 390, 920
- Oke, J. B., & Gunn, J. E. 1983, *ApJ*, 266, 713
- Osterbrock, D. E. 1989, *Astrophysics of Gaseous Nebulae and Active Galactic Nuclei* (Mill Valley, CA: University Science Books)
- Ota, K., Iye, M., Kashikawa, N., et al. 2008, *ApJ*, 677, 12
- Ota, K., Iye, M., Kashikawa, N., et al. 2010, *ApJ*, 722, 803
- Ouchi, M., Shimasaku, K., Akiyama, M., et al. 2008, *ApJS*, 176, 301
- Ouchi, M., Shimasaku, K., Furusawa, H., et al. 2003, *ApJ*, 582, 60
- Ouchi, M., Shimasaku, K., Furusawa, H., et al. 2010, *ApJ*, 723, 869
- Ouchi, M., Shimasaku, K., Okamura, S., et al. 2004, *ApJ*, 611, 660
- Padoan, P., Nordlund, A., & Jones, B. J. T. 1997, *MNRAS*, 288, 145
- Pawlik, A. H., Milosavljević, M., & Bromm, V. 2013, *ApJ*, 767, 59
- Pawlik, A. H., & Schaye, J. 2009, *MNRAS*, 396, L46
- Pawlik, A. H., Schaye, J., & van Scherpenzeel, E. 2009, *MNRAS*, 394, 1812
- Pei, Y. C. 1992, *ApJ*, 395, 130
- Planck Collaboration, Ade, P. A. R., Aghanim, N., et al. 2013a, arXiv:1303.5075
- Planck Collaboration, Ade, P. A. R., Aghanim, N., et al. 2013b, arXiv:1303.5076
- Press, W. H., & Schechter, P. 1974, *ApJ*, 187, 425
- Raičević, M., Theuns, T., & Lacey, C. 2011, *MNRAS*, 410, 775
- Rauch, M., Haehnelt, M., Bunker, A., et al. 2008, *ApJ*, 681, 856
- Reddy, N. A., & Steidel, C. C. 2009, *ApJ*, 692, 778
- Robertson, B. E., Furlanetto, S. R., Schneider, E., et al. 2013, *ApJ*, 768, 71
- Rodighiero, G., Vaccari, M., Franceschini, A., et al. 2010, *A&A*, 515, A8
- Romano, D., Silva, L., Matteucci, F., & Danese, L. 2002, *MNRAS*, 334, 444
- Salim, S., & Lee, J. C. 2012, *ApJ*, 758, 134
- Salvaterra, R., Ferrara, A., & Dayal, P. 2011, *MNRAS*, 414, 847
- Samui, S., Srianand, R., & Subramanian, K. 2009, *MNRAS*, 398, 2061
- Santos, M. R. 2004, *MNRAS*, 349, 1137
- Sasaki, S. 1994, *PASJ*, 46, 427
- Sawicki, M., & Thompson, D. 2006a, *ApJ*, 642, 653
- Sawicki, M., & Thompson, D. 2006b, *ApJ*, 648, 299
- Schenker, M. A., Robertson, B. E., Ellis, R. S., et al. 2013, *ApJ*, 768, 196
- Schiminovich, D., Ilbert, O., Arnouts, S., et al. 2005, *ApJL*, 619, L47
- Shankar, F., Lapi, A., Salucci, P., De Zotti, G., & Danese, L. 2006, *ApJ*, 643, 14
- Shapley, A. E., Steidel, C. C., Adelberger, K. L., et al. 2001, *ApJ*, 562, 95
- Sheth, R. K., & Tormen, G. 1999, *MNRAS*, 308, 119
- Shibuya, T., Kashikawa, N., Ota, K., et al. 2012, *ApJ*, 752, 114
- Shimasaku, K., Kashikawa, N., Doi, M., et al. 2006, *PASJ*, 58, 313
- Shull, J. M., Harness, A., Trenti, M., & Smith, B. D. 2012, *ApJ*, 747, 100
- Silk, J., & Mamon, G. A. 2012, *RA&A*, 12, 917
- Smit, R., Bouwens, R. J., Franx, M., et al. 2012, *ApJ*, 756, 14
- Sobacchi, E., & Mesinger, A. 2013, *MNRAS*, 432, L51
- Sobral, D., Best, P. N., Geach, J. E., et al. 2009, *MNRAS*, 398, 68
- Stanway, E. R., McMahon, R. G., & Bunker, A. J. 2005, *MNRAS*, 359, 1184
- Stark, D. P., Ellis, R. S., Bunker, A., et al. 2009, *ApJ*, 697, 1493
- Stark, D. P., Schenker, M. A., Ellis, R., et al. 2013, *ApJ*, 763, 129

- Steidel, C. C., Adelberger, K. L., Giavalisco, M., Dickinson, M., & Pettini, M. 1999, [ApJ](#), **519**, 1
- Sutherland, R. S., & Dopita, M. A. 1993, [ApJS](#), **88**, 253
- Tacchella, S., Trenti, M., & Carollo, C.-M. 2013, [ApJL](#), **768**, L37
- Tilvi, V., Malhotra, S., Rhoads, J. E., et al. 2009, [ApJ](#), **704**, 724
- Trenti, M., Stiavelli, M., Bouwens, R. J., et al. 2010, [ApJL](#), **714**, L202
- van Breukelen, C., Jarvis, M. J., & Venemans, B. P. 2005, [MNRAS](#), **359**, 895
- Vanzella, E., Giavalisco, M., Inoue, A. K., et al. 2010, [ApJ](#), **725**, 1011
- Wang, J., Navarro, J. F., Frenk, C. S., et al. 2011, [MNRAS](#), **413**, 1373
- Wyder, T. K., Treyer, M. A., Milliard, B., et al. 2005, [ApJL](#), **619**, L15
- Wyithe, J. S. B., & Bolton, J. S. 2011, [MNRAS](#), **412**, 1926
- Wyithe, J. S. B., & Loeb, A. 2013, [MNRAS](#), **428**, 2741
- Xia, J.-Q., Negrello, M., Lapi, A., et al. 2012, [MNRAS](#), **422**, 1324
- Yan, H., Finkelstein, S. L., Huang, K. H., et al. 2012, [ApJ](#), **761**, 177
- Yan, H., Yan, L., Zamojski, M. A., et al. 2011, [ApJL](#), **728**, L22
- Yoshida, M., Shimasaku, K., Kashikawa, N., et al. 2006, [ApJ](#), **653**, 988
- Zhao, D. H., Mo, H. J., Jing, Y. P., & Börner, G. 2003, [MNRAS](#), **339**, 12
- Zheng, Z.-Y., Finkelstein, S. L., Finkelstein, K., et al. 2013, [MNRAS](#), **431**, 3589